THE UNIVERSITY OF

ARIZONA

TUCSON ARIZONA

Final Technical Report

ONR Grant No. N00014-91-J-1797

"COMPUTATIONAL AND EXPERIMENTAL
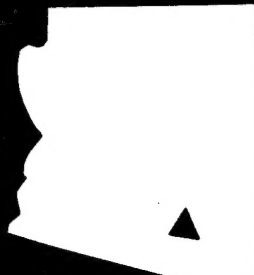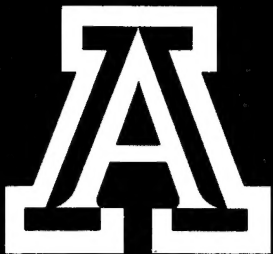INVESTIGATION OF TRANSITION
CONTROL IN BOUNDARY LAYERS"

Receptivity of a Flat Plate
Boundary Layer to Free-Stream
Pressure Waves

by

Hermann F. Fasel & Hubert L. Meitz

Department of Aerospace
and Mechanical Engineering
The University of Arizona
Tucson, Arizona 85721

19950612 017

ENGINEERING EXPERIMENT STATION
COLLEGE OF ENGINEERING AND MINES

THE UNIVERSITY OF ARIZONA

TUCSON, ARIZONA 85721

REPORT DOCUMENTATION PAGE

Public reporting burden for this collection of information is estimated to average 1 hour per response, including the time for reviewing instructions, searching existing data sources, gathering and maintaining the data needed, and completing and reviewing the collection of information. Send comments regarding this burden estimate or any other aspect of this collection of information, including suggestions for reducing this burden, to Washington Headquarters Services, Directorate for Information Operations and Reports, 1215 Jefferson Davis Highway, Suite 1204, Arlington, VA 22202-4302, and to the Office of Management and Budget, Paperwork Reduction Project (0704-0188), Washington, DC 20503.

1. AGENCY USE ONLY (Leave blank)	2. REPORT DATE	3. REPORT TYPE AND DATES COVERED
	June 6, 1995	Final Technical Report

4. TITLE AND SUBTITLE
Computational and Experimental Investigation of Transition Control in Boundary Layers

5. FUNDING NUMBERS
N00014-91-J-1787

6. AUTHOR(S)
Hermann F. Fasel and Hubert L. Meitz

7. PERFORMING ORGANIZATION NAME(S) AND ADDRESS(ES)
Department of Aerospace and Mechanical Engineering
College of Engineering and Mines
The University of Arizona
Tucson, Arizona 85721

8. PERFORMING ORGANIZATION REPORT NUMBER

9. SPONSORING/MONITORING AGENCY NAME(S) AND ADDRESS(ES)
Department of the Navy
Office of the Chief of Naval Research
800 N. Quincy Street, Code 1513:GNP
Arlington, VA 22217-5000

10. SPONSORING/MONITORING AGENCY REPORT NUMBER

11. SUPPLEMENTARY NOTES

12a. DISTRIBUTION/AVAILABILITY STATEMENT
Approved for Public release: Distribution is unlimited

12b. DISTRIBUTION CODE

13. ABSTRACT (Maximum 200 words)

A numerical simulation of a receptivity experiment by Kendall (1987) was performed, solving the 2-D, incompressible Navier-Stokes equations for a flat plate boundary layer. Emphasis was placed on the investigation of the mechanism that lead to the shift of energy from low frequencies to higher frequencies and to the different output/input ratios for different cylinder diameters in the experiment. The rotating cylinders that were used in the experiment to generate disturbances in the freestream were modeled by a numerical forcing function at the freestream boundary. It was found that the low frequency components of the induced disturbances, together with the steady flow, form a new, transient "baseflow" for disturbances with higher frequencies. It was demonstrated how the changing receptivity and stability characteristics of this "baseflow" lead to distinct peaks in the wavepackets that are generated by the freestream disturbance. Further investigation showed that the different output/input ratios can essentially be explained by the different amplitudes of the lowest frequencies in the forcing. Finally, a numerical experiment was performed with only two frequency components present in the forcing function. The validity of the proposed mechanism was confirmed by comparison of the results of this numerical experiment with those calculated from linear stability theory for the transient "baseflow".

14. SUBJECT TERMS

DTIC QUALITY INSPECTED 3

15. NUMBER OF PAGES
79

16. PRICE CODE

17. SECURITY CLASSIFICATION OF REPORT	18. SECURITY CLASSIFICATION OF THIS PAGE	19. SECURITY CLASSIFICATION OF ABSTRACT	20. LIMITATION OF ABSTRACT
Unclassified	Unclassified	Unclassified	UL

Final Technical Report
ONR Grant N00014-91-J-1787

"Computational and Experimental Investigation of
Transition Control in Boundary Layers"

Receptivity of a Flat Plate Boundary Layer
to Free-Stream Pressure Waves

by

Hermann F. Fasel, Hubert L. Meitz

Department of Aerospace and Mechanical Engineering
The University of Arizona
Tucson, AZ 85721

Accesion For		
NTIS CRA&I	☑	
DTIC TAB	☐	
Unannounced	☐	
Justification		
By		
Distribution /		
Availability Codes		
Dist	Avail and / or Special	
A-1		

Abstract

A numerical simulation of a receptivity experiment by Kendall (1987) was performed, solving the 2-D, incompressible Navier-Stokes equations for a flat plate boundary layer. Emphasis was placed on the investigation of the mechanism that lead to the shift of energy from low frequencies to higher frequencies and to the different output/input ratios for different cylinder diameters in the experiment. The rotating cylinders that were used in the experiment to generate disturbances in the freestream were modeled by a numerical forcing function at the freestream boundary. It was found that the low frequency components of the induced disturbances, together with the steady flow, form a new, transient "baseflow" for disturbances with higher frequencies. It was demonstrated how the changing receptivity and stability characteristics of this "baseflow" lead to distinct peaks in the wavepackets that are generated by the freestream disturbance. Further investigation showed that the different output/input ratios can essentially be explained by the different amplitudes of the lowest frequencies in the forcing. Finally, a numerical experiment was performed with only two frequency components present in the forcing function. The validity of the proposed mechanism was confirmed by comparison of the results of this numerical experiment with those calculated from linear stability theory for the transient "baseflow".

Table of Contents

Problem Statement and Overview

The subject of this research was a numerical simulation of an experiment carried out by Kendall (1987). In a low speed windtunnel, he studied the receptivity of a flat-plate boundary layer to an unsteady, traveling pressure field. The experiment provided some insight into the receptivity mechanism, but several open questions remained. Therefore it was hoped that a computer simulation would lead to a more detailed explanation of the specific receptivity path. Since the experimental data available were not sufficient to perform a quantitatively exact simulation, the main purpose of this work was to gain a deeper insight into the physical processes involved and to reach a qualitative understanding.

Chapter 1 of this report is a short introduction to the field of receptivity. In chapter 2, a summary of Kendall's experiment is given, covering the experimental setup and the principal results. Chapter 3 contains the Navier-Stokes equations that describe the physical problem, and their transformation to a more computer oriented form, the vorticity transport equation. The initial and boundary conditions chosen for the simulation are given in chapter 4. Since the numerical method was already described in great detail by others, it will be treated briefly in chapter 5.

The results of the simulation are discussed in chapter 6: The numerical model for the forcing is explained, and the data of the boundary layer response are analyzed and compared with those obtained in the experiment by Kendall. This analysis leads to a model of the receptivity mechanism which is presented in chapter 7.

In chapter 8, the concept of this mechanism is tested in two numerical experiments, and it is found to be valid.

Conclusions based on the results of chapters 7 and 8 are presented in chapter 9.

1.   Introduction

The laminar-turbulent transition in a boundary layer is in many cases initiated by a process which is now generally referred to as receptivity: This term denotes the various mechanisms by which disturbances in a boundary layer are forced by external perturbations such as surface roughness, sound, freestream turbulence, or unsteady pressure gradients.

For years receptivity was investigated mostly through experiments, and there were very few theoretical or numerical approaches. By now several theoretical models have led to an explanation for some important receptivity paths, although they are still widely disputed in the transition community. Recent overviews and summaries of receptivity experiments and theories are given by Nishioka and Morkovin (1986), Morkovin (1988) and Kerschen (1989).

In general, receptivity can affect transition in a boundary layer in two ways:

I.   The external perturbations create (small) disturbances inside the boundary layer. These are then amplified by instability mechanisms that depend only on the boundary layer flow itself and not on the external perturbations. In particular, the amplification of those disturbances is in the first stage accurately described by the classical linear stability theory. However, because the linear stability theory leads to an eigenvalue problem (the Orr-Sommerfeld equation), it can only predict the amplification rates of the disturbance waves, but not their absolute amplitudes. It is the receptivity process that provides the coupling between the magnitude of the external perturbations and the amplitudes of the Tollmien-Schlichting waves (the eigenfunctions of the Orr-Sommerfeld equation) in the boundary layer.

II. The external perturbations change the growth of disturbances already present in a boundary layer. In this case, the linear stability theory must at least be modified, or it may not be valid at all.

Sometimes there is a combination of both effects. In particular, if the external disturbances are very strong, receptivity can lead to immediate transition, bypassing the usual sequence of instability, amplification and breakdown.

The subject of the present work is the receptivity of a laminar boundary layer to unsteady pressure gradients. These are essentially inviscid fluctuations of the mean flow outside the boundary layer. Such fluctuations are always present in windtunnels, generated by fans and grids, or by turbulent boundary layers at the tunnel walls. In aircraft, they are generated by propellers or rotors, or by vibrations of the engine nacelles.

Unsteady pressure gradients can cover a wide range of phase speeds and frequencies. They are called spatially localized if the forcing is extended over very few wavelengths only (such as sound a from loudspeaker mounted close to a plate in a windtunnel). They are called global if the forcing is extended over a larger region (such as fluctuations produced by the windtunnel fan).

If the amplitudes of the pressure fluctuations are not too high, there must be a match of both temporal scales (i.e. frequency) and spatial scales (i.e. wavelength)

to produce positive receptivity. Here one can distinguish between two classes of receptivity:

A: A close match of phase speed between forcing disturbance and TS-waves

For a given frequency, this implies that the wavelengths of the forcing disturbance and of the eigenfunctions (the TS-waves) are the same, or are at least very close: $\lambda_{FS} \approx \lambda_{TS}$. This induces a resonance-like response of the boundary layer. In the theoretical model, the eigenvalue problem of the linear stability theory with homogeneous boundary conditions is replaced by a boundary value problem where the disturbance amplitude is enforced at the freestream boundary. Due to the match of wavelengths, this receptivity process works both with local and global excitations.

B: Different phase speeds of forcing disturbance and TS-waves

In this case, the wavelengths do not match, and either $\lambda_{FS} \ll \lambda_{TS}$ or, most often, $\lambda_{FS} \gg \lambda_{TS}$. A global forcing with a given frequency could still create disturbances inside the boundary layer, but the phases of those disturbances would cancel over one wavelength. In a boundary layer with slow streamwise variation of the mean flow (parallel flow assumption of linear stability theory), this amounts to a mere superposition of external perturbation and boundary layer flow, without any major interactions. An example for this case is sound excitation of a flow with very low Mach number.

Things are different, however, if the spatial extension of the forcing is not global but local (over very few wavelengths only). Here the necessary match of spatial scales is brought in by the length scale of the effective forcing region, through the forcing amplitude A(x). Receptivity to disturbances with non-matching wavelengths is also possible in regions with rapid streamwise variations of the boundary layer flow, such as near the leading edge, near steps, or near slots for suction/blowing: In this case there can be a match of spatial scales through a characteristic length L of the boundary layer change in x. Additionally, a rapid streamwise variation of the mean flow always means important nonlinearities in the governing equations, which can drastically enhance receptivity. This can possibly lead to a breakdown of long wavelengths of sound to the short wavelengths of TS-waves, a theory which is still disputed.

In the receptivity problem examined in this work, there is a close match of phase speed between the forcing and the TS-waves. One can therefore expect that the boundary layer response will be dominantly of a resonance type.

2.   Summary of Kendall's Experiment

2.1.   Experimental Setup

Kendall performed the experiment described here to study the mechanisms by which a traveling pressure field in the freestream excites TS waves in a boundary layer. He installed a rotor-like assembly in a low-speed windtunnel close to a flat plate, as illustrated in Fig.1 (Kendall (1987), Fig. 2). The rotor consisted of two rods (thin cylinders) mounted parallel to each other on opposite ends of two rotating arms, with the axis of the rotation being parallel to the plate and normal to the flow. The closest approach of the rods to the plate was several times the local boundary layer thickness. Thus the boundary layer sensed only the irrotational disturbance field due to the relative movement of the cylinders and did not sense the influence of their viscous wakes.

This setup produced periodic pressure fluctuations in the freestream just outside the boundary layer, traveling at about the circumferential speed U_c of the rods. These pressure fluctuations excited wave packet-like disturbances inside the boundary layer. The circumferential velocity of the rods could be varied over a certain range, and it turned out that a ratio U_c/U_∞ of around 1/3 produced the strongest response in the boundary layer. That velocity was close to the phase speed of the most unstable TS waves for the local Reynolds number.

The nature of the forcing-field was determined by hot-wire measurements outside the boundary layer. Hot-wire measurements were also made inside the boundary layer to determine the response to the forcing. The obtained data were then Fourier transformed to analyze the frequency composition of both the forcing and the response: Any component of the Fourier transform will be referred to as 'mode n', indicating that its frequency F_n is $n \times F_1$. The fundamental frequency F_1 was twice the circular frequency of the rotor, because each of the two rods induced identical disturbances. Kendall reported data for modes 1 to 12; and amplified TS waves are expected within the range of modes 6 to 12, depending on the distance from the leading edge.

2.2.   Experimental Results

The forcing region extends over 15 to 20 cm for the higher modes and over a larger domain for the lower modes, demonstrated through the amplitudes plotted in Fig.4 (Kendall (1987), Fig. 8a).

The streamwise development of the induced disturbance signal is plotted in Fig.11 (Kendall (1987), Fig. 11). These curves demonstrate the wave packet-like nature of the disturbances. The evolution of rather sharp peaks downstream of the rotor indicates a shift of energy from low frequencies to higher frequencies. Kendall did not further investigate the mechanism of this energy transfer and gave no interpretation of it.

The amplitudes of the boundary layer response, measured at the vertical location of the strongest fluctuation, are shown in Fig.13 (Kendall (1987), Fig. 13). Upstream of the rotor station, all modes are strongly amplified. Downstream of

the rotor, the lowest modes (1 – 4) start to decay, whereas the higher modes (the unstable TS-components) keep growing. The amplitudes of the highest modes (11, 12) exhibit strong growth downstream of the rotor station until they reach a local maximum. After this maximum they decay over a short distance, but start to grow again at the end of the observed region. The reason for this amplitude growth is not quite clear from the experimental data.

To evaluate the efficiency of the forcing mechanism, Kendall divided the amplitudes of the boundary layer response at a downstream location ($\sim$ output) by the forcing amplitudes ($\sim$ input). The (output/input) ratios for two different rod diameters are plotted in Fig.30 (Kendall (1987), Fig. 15). The greater "efficiency" of the larger rods for the higher frequencies is evident: With the bigger rods, the higher modes are amplified more strongly, and the maximum of the (output/input) ratio is shifted to a higher frequency. There is no straightforward explanation for this difference.

To gain insight into the receptivity processes just discussed, numerical simulations of this experiment were performed. In particular, from the simulations we hoped to find answers to the following questions:

1.) What is the mechanism by which the disturbances induced by the rods are transformed into TS waves inside the boundary layer?

2.) Can the shift of energy from lower frequencies to higher frequencies be explained by linear stability theory? If not, what other mechanisms contribute to it?

3.) What is the reason for the different (output/input) ratios obtained with the two different rod diameters?

3. Governing Equations

The numerical simulation was carried out under the assumption that compressibility and 3-D effects could be neglected. Thus, the governing equations to be solved were the incompressible, 2-D Navier Stokes equations. In their basic, primitive variable form they consist of the two momentum equations (1.1) and of the continuity equation (1.2).

$$\frac{\partial \hat{u}}{\partial \hat{t}} + \hat{u}\frac{\partial \hat{u}}{\partial \hat{x}} + \hat{v}\frac{\partial \hat{u}}{\partial \hat{y}} = -\frac{1}{\hat{\rho}}\frac{\partial \hat{p}}{\partial \hat{x}} + \nu\left(\frac{\partial^2 \hat{u}}{\partial \hat{x}^2} + \frac{\partial^2 \hat{u}}{\partial \hat{y}^2}\right) \qquad (1.1\ a)$$

$$\frac{\partial \hat{v}}{\partial \hat{t}} + \hat{u}\frac{\partial \hat{v}}{\partial \hat{x}} + \hat{v}\frac{\partial \hat{v}}{\partial \hat{y}} = -\frac{1}{\hat{\rho}}\frac{\partial \hat{p}}{\partial \hat{y}} + \nu\left(\frac{\partial^2 \hat{v}}{\partial \hat{x}^2} + \frac{\partial^2 \hat{v}}{\partial \hat{y}^2}\right) \qquad (1.1\ b)$$

$$\frac{\partial \hat{u}}{\partial \hat{x}} + \frac{\partial \hat{v}}{\partial \hat{y}} = 0 \qquad (1.2)$$

where:

$\hat{t}$: time	$\hat{u}$: streamwise velocity
$\hat{x}$: streamwise coordinate	$\hat{v}$: normal velocity
$\hat{y}$: normal coordinate	$\hat{p}$: pressure
ν : dynamic viscosity	$\hat{\rho}$: density

Equations (1.1) and (1.2) are in dimensional form. Nondimensionalization of the basic variables allows for a more efficient computation. To account for the boundary layer characteristics of the flow, the normal coordinate y and the normal velocity v are stretched by the factor $\sqrt{Re}$.

The nondimensionalized variables are:

$$Re = \frac{U_\infty L}{\nu} \qquad \begin{aligned} x &= \frac{\hat{x}}{L} & y &= \frac{\hat{y}}{L}\sqrt{Re} & t &= \frac{\hat{t}\,U_\infty}{L} \\[2mm] u &= \frac{\hat{u}}{U_\infty} & v &= \frac{\hat{v}}{U_\infty}\sqrt{Re} & p &= \frac{\hat{p}}{\hat{\rho}\,U_\infty^2} \end{aligned} \qquad (1.3)$$

where:

U_∞ : freestream velocity

L : a characteristic length

Thus the basic equations in nondimensional form are:

$$\frac{\partial u}{\partial t} + u\frac{\partial u}{\partial x} + v\frac{\partial u}{\partial y} = -\frac{\partial p}{\partial x} + \frac{1}{Re}\frac{\partial^2 u}{\partial x^2} + \frac{\partial^2 u}{\partial y^2} \qquad (1.4\ a)$$

$$\frac{\partial v}{\partial t} + u\frac{\partial v}{\partial x} + v\frac{\partial v}{\partial y} = -\frac{\partial p}{\partial y} + \frac{1}{Re}\frac{\partial^2 v}{\partial x^2} + \frac{\partial^2 v}{\partial y^2} \qquad (1.4\ b)$$

$$\frac{\partial u}{\partial x} + \frac{\partial v}{\partial y} = 0 \ . \qquad (1.5)$$

Differentiating eqns.(1.4) with respect to x and y, subtracting (1.4b) from (1.4a) and introducing the vorticity ω

$$\omega = \frac{\partial u}{\partial y} - \frac{1}{Re}\frac{\partial v}{\partial x} \qquad (1.6)$$

where:

$$\omega = \frac{\hat{\omega}L}{U_\infty\sqrt{Re}} \qquad (1.7)$$

yields the vorticity transport equation:

$$\frac{\partial \omega}{\partial t} + u\frac{\partial \omega}{\partial x} + v\frac{\partial \omega}{\partial y} = \frac{1}{Re}\frac{\partial^2 \omega}{\partial x^2} + \frac{\partial^2 \omega}{\partial y^2} \ . \qquad (1.8)$$

Differentiating eq.(1.6) with respect to x and y, and using eq.(1.5) leads to two Poisson equations for u and v:

$$-\frac{\partial \omega}{\partial x} = \frac{1}{Re}\frac{\partial^2 v}{\partial x^2} + \frac{\partial^2 v}{\partial y^2} \qquad (1.9\ a)$$

$$\frac{\partial \omega}{\partial y} = \frac{1}{Re}\frac{\partial^2 u}{\partial x^2} + \frac{\partial^2 u}{\partial y^2} \ . \qquad (1.9\ b)$$

Alternatively, u can be calculated from v, using eq.(1.5) and differentiating with respect to x:

$$\frac{\partial^2 u}{\partial x^2} = -\frac{\partial^2 v}{\partial x \partial y} \qquad (1.9\ c)$$

This formulation is better suited for a numerical method.

4.   Integration Domain, Initial and Boundary Conditions

4.1.   Integration Domain

For the numerical simulation, a rectangular domain was cut out of the entire physical flow field. It is in this domain where the essential process of receptivity takes place. In the computation it is represented by a rectangular $(M \times N)$ grid (Fig.2).

The boundaries are:

Inflow Boundary A–D

$$n = 1; \quad m = 1, \ldots, M; \quad x = x_0$$

Surface of the Plate A–B

$$n = 1, \ldots, N; \quad m = 1; \quad y = 0$$

Outflow Boundary B–C

$$n = N; \quad m = 1, \ldots, M; \quad x = x_e$$

Freestream Boundary D–C

$$n = 1, \ldots, N; \quad m = M; \quad y = Y$$

4.2.   Initial Conditions

The vorticity transport equation is of parabolic type with respect to t, therefore initial conditions must be prescribed in the whole integration domain.

$$
\begin{aligned}
u(x, y, 0) &= u_0(x, y) \\
v(x, y, 0) &= v_0(x, y) \\
\omega(x, y, 0) &= \omega_0(x, y)
\end{aligned}
\tag{1.10}
$$

where u_0, v_0, ω_0 denote the values of the steady-state solution of a zero-pressure gradient flow over a flat plate.

4.3. Boundary Conditions

Ideally, the boundaries would be at infinity (except for the plate surface), with all disturbance quantities set to zero, and the values of u, v and ω would be prescribed at all boundaries. The numerical method, however, allows only for a limited integration domain, where the values at the boundaries are part of the solution. Hence, the boundary conditions are not quite straightforward. After several numerical tests, the boundary conditions given by Fasel (1976) were applied at the inflow and outflow boundaries and at the surface of the plate. The freestream boundary condition was adopted from Gruber (1986).

Inflow boundary A-D

$$
\begin{aligned}
u(x_0, y, t) &= u_B(x_0, y) \\
v(x_0, y, t) &= v_B(x_0, y) \\
\omega(x_0, y, t) &= \omega_B(x_0, y)
\end{aligned}
\tag{1.11}
$$

where u_B, v_B, ω_B denote the Blasius solution of the boundary layer equations. Within the desired accuracy, this is identical to the solution of the full Navier-Stokes equations. The inflow conditions are kept constant throughout the computation.

Surface of the Plate A-B

$$
\begin{aligned}
u(x, 0, t) &= 0 \\
v(x, 0, t) &= 0 \\
\left. \frac{\partial \omega}{\partial x} \right|_{(x,0,t)} &= \left. \frac{\partial^2 v}{\partial y^2} \right|_{(x,0,t)}
\end{aligned}
\tag{1.12}
$$

The no-slip condition at the non-permeable wall imposes zero velocity. The condition for ω follows from (1.9 a).

Outflow Boundary B-C

$$
\begin{aligned}
\left. \frac{\partial^2 u}{\partial x^2} \right|_{(x_e, y, t)} &= -\alpha^2\, u'(x_e, y, t) \\
\left. \frac{\partial^2 v}{\partial x^2} \right|_{(x_e, y, t)} &= -\alpha^2\, v'(x_e, y, t) \\
\left. \frac{\partial^2 \omega}{\partial x^2} \right|_{(x_e, y, t)} &= -\alpha^2\, \omega'(x_e, y, t)
\end{aligned}
\tag{1.13}
$$

where the primes denote the disturbance-flow quantities:

$$
\begin{aligned}
u'(x, y, t) &= u(x, y, t) - u_0(x, y) \\
v'(x, y, t) &= v(x, y, t) - v_0(x, y) \\
\omega'(x, y, t) &= \omega(x, y, t) - \omega_0(x, y)
\end{aligned}
\tag{1.14}
$$

These conditions allow a wave of wavenumber α to pass through the right boundary, assuming $\partial^2/\partial x^2(u_0,v_0,\omega_0)\big|_{x_e,y}= 0$ for all baseflow quantities. In the numerical simulation, α was the wavenumber of the Tollmien-Schlichting wave with the highest amplitude at the outflow boundary.

A difficulty arose during the first computations. The amplitudes at the peaks of the induced wave packets were very high at the end of the integration domain, and the line iteration did not converge when a peak arrived at the outflow-boundary. The remedy was as follows: At the end of the region to be observed ($N_E = 499$), a so called "damping" domain was added from $n = 500$ to $N = 700$. But instead of a flat plate baseflow (corresponding to a Falkner-Skan parameter $\beta_{FS} = 0$), a baseflow with strong favorable pressure gradient was imposed ($\beta_{FS} = 1$). There were no feedback effects upstream, and all disturbances were so strongly damped that no further convergence problems arose.

<u>Freestream Boundary D-C</u>

$$
\begin{aligned}
u(x,Y,t) &= U(x,t) \\
\frac{\partial v}{\partial y}\bigg|_{(x,Y,t)} &= -\frac{\partial U}{\partial x}\bigg|_{(x,t)} \\
\omega(x,Y,t) &= 0
\end{aligned}
\tag{1.15}
$$

With $U(x,t)$ an arbitrary function can be imposed. The condition $\partial v/\partial y$ follows from the continuity equation (1.5). Assuming irrotational flow outside of the boundary layer, $\omega = 0$ is imposed at the boundary.

5. Numerical Method

Most of the results presented in this paper were obtained using a finite difference method that was developed for the investigation of the laminar-turbulent transition in a flat plate boundary layer. It was based on a method developed by Fasel (1976) and is described in detail by Rist (1990).

The x and y derivatives in eqs. (1.8) and (1.9) are discretized using fourth-order accurate finite-difference approximations. In order to maintain consistency and an overall fourth-order accuracy, it is necessary to integrate the boundary conditions into the discretization of the equations at the gridlines adjacent to the boundaries. This is discussed in detail by Fasel (1979). The time derivative $\partial\omega/\partial t$ in the vorticity transport equation (1.8) is discretized using a third order Adams-Bashforth approximation. Thus, the method is explicit, and the values for ω at a new timestep are easily computed from the data of the previous timesteps.

The equation for v (1.9 a) is discretized using standard fourth-order differences for the x and y derivatives. At every timestep the resulting system of equations is solved by line iteration (SLOR). To account for the boundary layer characteristics of the flow, the y direction is treated such that the unknowns on lines $n = constant$ parallel to the y coordinate are obtained by direct solution of a pentadiagonal system of equations. The iteration proceeds in x direction, marching downstream from the inflow boundary at every iteration sweep (see Fig.3).

In order to fully exploit the vector-processing capabilities of the supercomputer used for these calculations, a modified "Zebra" line-iteration is used. Every iteration step is split up into three sweeps, starting at $n = 3, 4, 5$, respectively, and advancing in x by three gridlines each time the equation has been solved for a line $n = constant$. This is necessary because the computational stencil for v requires the values on the lines $n - 2, n - 1$ and $n + 1, n + 2$ for the x derivative. Vectorization of the sweeps, however, does not allow the use of data of the lines $n - 2, n - 1$ for the solution of line n.

Thus, at iteration level i, the first sweep computes the new values for v on gridlines $n = 3, 6, 9, ...$, using the old values of iteration level $i - 1$ on gridlines $n - 2, n - 1, n + 1, n + 2$. This avoids a recursive dependence and allows for vectorization. The second sweep computes the new values on gridlines $n = 4, 7, 10, ...$, using the values of the first sweep on gridlines $n - 1, n + 2$, and the old values of iteration level $i - 1$ on gridlines $n - 2, n + 1$. The third sweep computes the new values on gridlines $n = 5, 8, 11, ...$, using the values of the first and second sweep on gridlines $n - 2, n - 1, n + 1, n + 2$. Overrelaxation is performed after every sweep. The values on gridlines $n = 2, n = N - 1, n = N$ are computed separately at each iteration level in order to account for the boundary conditions, and at $n = 1$ the Blasius solutions are prescribed.

The equation for u (1.9 c) is discretized using fourth-order accurate compact differences, and the resulting tridiagonal system of equations is solved using the standard Thomas algorithm.

Some of the results were confirmed using another method, namely an implicit method which was also based on the original method of Fasel (1976). For this,

the discretization of the spatial derivatives is essentially the same as in the explicit method described above. Instead of equation (1.9 c), equation (1.9 b) is used for the calculation of u. The $\partial\omega/\partial t$ term in the vorticity transport equation (1.8) is discretized using a three point backward difference of second order accuracy, hence the method is fully implicit and the nonlinear terms are evaluated at the most recent timelevel. This discretization leads to a coupled, nonlinear system of equations for u, v, and ω. This system is solved at every timestep by a line iteration procedure, combining the iterations for all equations in one iteration loop.

6.   Numerical Results

6.1.   Modeling of the Forcing Field

In the numerical simulation, the forcing field due to the rotation of the two rods is replaced by imposing a forcing function $U(x,t)$ at the freestream boundary. This forcing function should model the following parameters for all modes:
-    amplitude (x,y)
-    phase (x,y)
-    phase speed (x,y)

The fact that the function is not precisely known a priori gives rise to two conflicting difficulties:

6.1.1.   Streamwise Modeling

First, the forcing field is exactly prescribed at one point underneath the rotor, at a vertical distance y of about two boundary layer thicknesses, by the Fourier coefficients given by Kendall (1987,I). For the rest of the forcing domain, the amplitudes and phases are approximately given as curves over x, at a constant distance y (Kendall (1987), Fig.8).

In the experiment, the phase speeds underneath the rotor of all modes were about $u_s = 0.9\,U_c$, U_c being the circumferential speed of the rods. The phase speeds at the upstream and downstream limits of the forcing region were considerably lower, this was due to the circular motion of the rods.

The forcing amplitudes measured by Kendall are plotted in Fig.4 (Kendall (1987), Fig. 8a). They are highest at the center station and decay further upstream and downstream near the edges of the forcing region. Thus the forcing with high amplitudes near the rotor is characterized by a phase speed that is almost constant, and most of the disturbance energy enters the boundary layer in this region of nearly constant phase speed.

For the numerical simulation it was therefore assumed that the variation of the phase speeds near the edges of the forcing region was not essential to the receptivity process. By imposing a constant phase speed throughout the forcing domain, one additional parameter was eliminated and the investigation of the receptivity mechanism was simplified.

The forcing to be imposed at the freestream boundary can be expressed through the function

$$U(x,t) = U_0 + \sum_l A_l(x)\,\psi_l\,\sin(\alpha_l x - \beta_l t + \phi_l) \qquad (1.16)$$

where:

$$U_0 \; : \; \text{freestream velocity of baseflow}$$
$$A_l(x) \; : \; \text{amplitude of mode } l$$
$$\psi_l \; : \; \text{factor due to extrapolation in y-direction}$$
$$\alpha_l = l \times \alpha_1 \; : \; \text{constant wavenumber of mode } l$$
$$\beta_l = l \times \beta_1 \; : \; \text{constant circular frequency of mode } l$$
$$\beta_1 \; : \; \text{circular freqequency of mode 1}$$
$$\alpha_1 = \beta_1/u_s \; : \; \text{wavenumber of mode 1}$$
$$\phi_l = \text{ATAN2}\,(\text{re}(c_l), -\text{im}(c_l))$$
$$c_l \; : \; \text{complex Fourier coefficient of mode } l$$

Here, ϕ_l is the relative phase of mode l at the rotor station $x = x_c$. The nondimensional freestream velocity is set to 1. As suggested by Kendall, a Gaussian distribution was adopted to model the amplitudes $A_l(x)$.

$$A_l(x) = a_l \, \exp\left(-b_l(x - x_c)^2\right) \qquad (1.17)$$

where:

$$a_l \; : \; \text{amplitude of mode } l \text{ at } x = x_c$$
$$x_c \; : \; \text{x-location underneath rotor-axis: } 0.66 \text{ m}$$

The parameters b_l were chosen such as to obtain the best fit of the Gaussian approximation with the amplitudes of Fig.4 . The coefficients b_l, ψ_l, c_l are given in Table 1, the amplitudes a_l are those given in Table 3. The forcing amplitudes in the numerical simulation are plotted in Fig.5.

There is a reasonable agreement of the forcing amplitudes in experiment and simulation. However, the forcing amplitudes of the highest modes are given only near the rotor station, and it is hoped that the Gaussian distributions further upstream and downstream are not too far off the realistic values.

The factor b_1 had to be chosen 50% smaller than it should have been according to the experimental data. This was done because otherwise the integration domain would have been too large for a practical computation, since the computation requires that all disturbances are zero at the inflow boundary. A necessary consequence of this restriction is that the fundamental mode 1 is not as strongly forced in the simulation as in the experiment.

6.1.2. Vertical Modeling

Second, the forcing is expected to generate TS waves inside the boundary layer that are subsequently convected downstream. Since their amplitudes decay exponentially outside the boundary layer, they are not yet negligible at a vertical distance of only two boundary layer thicknesses. Because the forcing function at that distance is only approximately given, one expects a superposition of the prescribed disturbance and the response of the boundary layer in the region downstream of the rotor.

It turned out that a way to account for this was to extend the integration domain in y-direction to about four to five boundary layer thicknesses. At the freestream boundary, the amplitudes of all response disturbances (the TS waves) are then set to zero. This restriction at such a distance should not too severely affect the development of TS waves closer to the wall.

The only disturbances allowed at the freestream boundary are those imposed by the forcing function $U(x,t)$. But because the data given by Kendall were measured at a distance much closer to the plate, extrapolation also in y-direction is necessary to provide realistic data at the distance further away.

The velocity amplitudes $u'(y)$ underneath the rotor axis are different for each mode (see Fig.18 at $n = 82$), and several numerical tests were necessary to obtain reasonably accurate amplitudes for all modes. The forcing amplitudes at the freestream boundary were then corrected through the factors ψ_l in eq.(1.16). Changes in the phases over y were so small that they could be neglected. It was also assumed that the coefficients b_l were unaffected by the difference in y-distance. The amplitudes, observed underneath the rotor at a vertical distance of about two boundary layer thicknesses (at $m = 51, n = 82$) are given in Table 2. For comparison, those measured by Kendall are given in Table 3.

The time signal of the u'-component of the forcing is shown in Fig.6. It is plotted over two periods, observed underneath the rotor station (at x=0.66 m) at two vertical locations, $m = 121$ (at the freestream boundary) and $m = 51$ (at a distance of about two boundary layer thicknesses).

6.2.   Boundary Layer Response

6.2.1.   Time Signal of Disturbance Flow

The disturbance velocities $u'(x,y)$ and $v'(x,y)$ and the disturbance vorticity $\omega'(x,y)$ are plotted in Fig.7, Fig.8 and Fig.9 for several timesteps. These perspective plots give a good impression of the generation of TS wave packets by the periodic forcing introduced at the freestream boundary. The vorticity plots in Fig.9 show the development of spikes, indicating a shift of energy to high frequency components.

The disturbance velocity u', observed at the vertical location of maximum fluctuation inside the boundary layer, is shown in Fig.10. The curves are plotted for several x-locations, starting at x=0.41 m, with increments of 12.3 cm. The third curve from the top shows the disturbance signal at the rotor station (at x=0.66 m), and the bottom curve the shows the disturbance signal at x=1.15 m. The successive vertical offset between each baseline corresponds to a disturbance velocity $u' = 1\%$. The corresponding data from the experiment are plotted in Fig.11 (Kendall (1987), Fig. 11). Compared to the curves from the simulation, it appears that in this figure each curve is upside down (also compared to Kendall's Fig. 14). Otherwise, qualitatively the curves from the experimental data agree very well with those from the numerical simulation.

The disturbance velocity u' at x=0.91 m, observed at the vertical location of the strongest fluctuation, is shown in Fig.12 (simulation) and Fig.13 (Kendall (1987), Fig. 14). Again, there is a good qualitative agreement between experiment

and simulation in the shape of the disturbance signals. But there are also some important quantitative differences. In the simulation, the overall fluctuation level is considerably lower than in the experiment. Also, in the simulation the "spikes" in the signal are not as distinct, indicating that the highest modes carry less energy than in the experiment.

6.2.2.   Amplitude Growth from Linear Stability Theory

To get a better understanding of the amplitude growth both in the experiment and in the simulation, it is useful to consider the amplitude growth predicted by linear stability theory. In Fig.14, the integration domain of the numerical simulation is shown relative to the neutral stability curve for the undisturbed baseflow (a zero pressure gradient flow over a flat plate).
According to this diagram, the following can be expected :

– All modes should be stable at the inflow boundary.
– The lowest modes $(1 - 4)$ should be stable over most of the region considered in experiment and simulation (up to x_{we}).
– The most amplified TS waves should be within the modes $6 - 10$, since these modes are inside the neutral stability curve throughout most of the computational domain.
– The highest modes $(11 - 15)$ should subsequently pass both the lower and upper branch of the neutral stability curve, and they should be damped at the end of the region considered here.

6.2.3.   Streamwise Amplitude Development

For further interpretation of the results, the time signals of the u' velocity were Fourier analyzed at every (x, y) gridpoint. The amplitudes of $u'(x, y)$ are plotted in Fig.15. Some characteristic differences between the stable lowest modes and the unstable higher modes can be observed. The amplitudes of the lowest modes grow in the region upstream of the rotor and decay thereaft. Apparently, their growth rates are essentially prescribed by the forcing.

The amplitudes of the higher modes 5–10 grow throughout the observed region once they are induced by the freestream forcing. The highest modes (stable downstream of the rotor) exhibit a rather irregular amplitude growth, with alternating growth and decay. A closer inspection reveals a strong modulation in streamwise direction. This is apparently due to an interference between the TS-waves and Stokes-type waves traveling at the forcing phase speed u_s, introduced through the nonlinear convective terms in the vorticity transport equation (see Appendix D). This amplitude modulation has been observed in several other experiments, and it is also present in the experimental data obtained by Kendall (see Fig.17). By smoothing out the variation due to the amplitude modulation, one obtains growing amplitudes of modes 11–15 all the way downstream of the rotor, even outside of the forcing region. This is not in agreement with linear stability theory for a steady flat plate boundary layer.

For comparison with Kendall's experimental data, the u' amplitudes $\log(A)$ at the vertical location of maximum fluctuation are plotted in Fig.16. The amplitudes

log (A/A_{ref}) measured by Kendall are shown in Fig.17. Here, $R=550$ corresponds to x=0.46 m and $R=850$ to x=1.0 m $(R=\sqrt{Re_x})$. Comparison shows good qualitative agreement of experiment and simulation. However, there are some important differences:

mode 1	In the simulation, the slope at the upstream limit of the forcing region (x=0.46 m) is steeper then in the experiment. Assuming a Gaussian amplitude distribution in both experiment and simulation, this indicates that the amplitude further upstream of the rotor is lower than in the experiment. This is a consequence of the lower exponent b_1 in the forcing function.
modes 5–15	In the simulation, the initial amplitudes at the beginning of the forcing are two to three orders of magnitudes lower than in the experiment. This is due to the fact that all disturbances are zero at the inflow boundary in the simulation, whereas a minimum background turbulence cannot be avoided in windtunnel experiments.
modes 11–15	In the simulation, the modulation of the amplitudes of modes 11 and 12 downstream of the rotor is not as distinct as in the experiment, although it clearly is present. Nevertheless, the amplitudes of the highest modes (13–15) are strongly modulated in the simulation. Apparently, the qualitative characteristics are the same as in the experiment, they are however somewhat shifted to the higher modes.

The amplitudes of $u'(y)$ are shown in Fig.18 for various x-locations. Since all fluctuations except the forcing were set to zero at the freestream boundary, a non-zero amplitude at $m = 121$ indicates that the particular mode was forced at that location.

$n= 42$	(x=0.41 m) The lowest modes are already forced, wheras higher modes exist only as very weak background fluctuation ("numerical noise").
$n= 82$	(x=0.66 m) This is the location of strongest forcing underneath the rotor station. The amplitude profiles of the lowest modes are similar to those of a Stokes-oscillation. The higher and highest modes (unstable) look like "forced eigenfuctions". Starting from the freestream boundary, the amplitudes decay until just outside the boundary layer. Inside the layer, the profiles are similar to those of Orr-Sommerfeld eigenfunctions (TS waves).
$n=122$	(x=0.91 m) The amplitudes of modes 1–12 show distinct eigenfunction profiles. The highest modes 13–15 exhibit some irregularities near the wall, this suggests a possible nonlinear development.
$n=162$	(x=1.15 m) The amplitudes of modes 3–11 show eigenfunction-like profiles. Those of the lowest modes 1,2 and of the highest modes 12–15 are somewhat irregular at the wall, again possibly indicating nonlinear effects.

6.2.4.   Streamwise Phase Development

The phase development of u' is shown in Fig.19. The continuous slopes of the phase curves of the lowest modes demonstrate that they have wave-like behavior already far upstream of the rotor. The higher and highest modes do not set in until shortly before the rotor station: Here, their respective forcing amplitudes have reached a certain threshold above the "numerical noise". This observation agrees well with the amplitude curves in Fig.16, where the higher amplitudes start growing only right under the rotor. The highest modes exhibit a slight change of phase speed downstream of the rotor, around x=0.9 m. This corresponds to the dents in the amplitude (x) curves, and to the irregularities observed in the amplitude (y) profiles in Fig.18.

6.2.5.   Comparison of Amplitudes in Experiment and Simulation

The time signals plotted in Fig.12 and Fig.13 show that the fluctuation level at the end of the forcing domain is considerably higher in the experiment than in the simulation. This is confirmed by the absolute values of the amplitudes, given in Table 4 and Table 5. These were recorded at the vertical location of maximum fluctuation, at x=0.91 m and $n = 122$, respectively. The experimental amplitudes are between 15% and 47% higher than those in the simulation. Also, the overall disturbance amplification in the simulation is equal to or higher than that in the experiment, yet the absolute amplitudes at the end of the forcing are lower (particularly those of the highest modes). There are several reasons for the differences:

(1.)   The amplitudes of the background fluctuations upstream of the forcing were higher in the experiment than in the simulation. In a windtunnel experiment, disturbances of any frequency are always present with some finite amplitudes, whereas in the simulation there were no disturbances introduced at the inflow boundary of the integration domain. This is likely to be the most important cause for the difference in the output amplitudes.

(2.)   The forcing of the fundamental mode 1 is not as strong in the simulation as in the experiment. Due to the nature of the energy transfer mechanism (described later), this has an important effect on the amplitudes of other modes as well.

(3.)   In the simulation, the forcing amplitudes of several modes at $n = 82$ (underneath the rotor) are somewhat smaller than in the experiment.

(4.)   The nature of the high frequency forcing downstream of the rotor station is not clear from the experimental data, the forcing imposed in the simulation may not be sufficient.

(5.)   A constant phase speed was assumed in the simulation, whereas the phase speeds in the experiment were lower at the edge of the forcing region.

The effects of point 4 and 5 are not very clear, and they may not be important for the receptivity process.

6.2.6. Evolution of Modes 1, 8 and 15

To gain further insight how the freestream disturbances excite the TS waves in the boundary layer, the amplitudes and phases of modes 1, 8 and 15 were examined at several x-locations. Mode 1 was chosen because it is dominant throughout most of the integration domain, and because it is the fundamental mode. Mode 8 was chosen because it is among the most unstable modes, with a strong amplification all the way downstream from the rotor station. At the end of the observed region, the amplitude of mode 8 is the highest of all modes. Mode 15 was chosen because it is the highest mode, and it is already past the neutral stability curve downstream of the rotor axis.

The phase speed of the forcing $u_s = 0.33\,U_\infty$ is very close to the phase speed of the eigenfunctions of the boundary layer (both stable and unstable ones). As a result, there is a close match of both wavelength and phase speed between the forcing disturbance and the particular eigenfunction (the response of the boundary layer) at any frequency. On the other hand, there are no rapid streamwise variations in the steady flow, which would enhance a breakdown of disturbances with long wavelengths into TS waves. Thus, one can expect resonance-like responses of the boundary layer. Depending on the frequency F_n of the disturbance and on the local Reynolds number Re_δ, the response is expected to be of one of three types:

(1.) Subcritical excitation. In the stability diagram (Fig.14), this case corresponds to a point (F_n, Re_δ) upstream of the lower branch of the neutral stability curve. (Mode 1)

(2.) Resonance excitation. This case corresponds to a point (F_n, Re_δ) between the upper and lower branches of the neutral stability curve. (Mode 8)

(3.) Supercritical excitation. This case corresponds to a point (F_n, Re_δ) downstream of the upper branch of the neutral stability curve. (Mode 15).

The amplitudes and phases of mode 1 are shown in Fig.20 and Fig.21. They are given at various x-locations, starting at x=0.41 m ($n = 42$), with an increment of 12.3 cm between subsequent stations. This case represents a "subcritical excitation": The induced disturbance wave starts out with a profile similar to that of a Stokes-type oscillation. At subsequent stations, the development of an eigenfunction-type profile is clearly observable. Since mode 1 is stable throughout the integration domain, its amplitude growth is largely due to the forcing itself. The amplitude inside the boundary layer starts to decay once the forcing amplitude decreases (downstream of the rotor). At x=1.03 m ($n = 142$), both amplitude and phase exhibit somewhat irregular behavior. At this location, the amplitudes of the other modes have reached such high levels that they affect the development of mode 1.

The amplitudes and phases of mode 8 are plotted in Fig.22 and Fig.23. Since mode 8 forcing is restricted to a smaller region than the forcing of mode 1, these curves are recorded at stations starting at x=0.54 m ($n = 62$). The spatial increment between subsequent x-locations is 3 cm. This case represents the "resonance excitation", because mode 8 is unstable throughout most of the integration domain. Again, the amplitudes and phases at the onset are similar to those of a Stokes-

oscillation wave. At subsequent stations, one can clearly observe the evolution of profiles that are reminiscent of "forced" eigensolutions, where the amplitude does not decay outside of the boundary layer but rises exponentially. Finally, the typical profiles of TS waves appear downstream of the forcing region.

The amplitudes and phases of mode 15 are plotted in Fig.24 and Fig.25. Curves are shown for stations starting at x=0.54 m ($n = 62$). The spatial increment between subsequent x-locations is 3 cm. Theoretically, this case represents the "supercritical excitation", because downstream of the rotor, the mode 15 eigensolutions are past the upper branch of the neutral stability curve, and the amplitude should decay. First, one can observe that mode 15 forcing sets in much later than mode 8 forcing. Once mode 15 disturbances are present, their profiles evolve rapidly into profiles of forced eigensolutions. Downstream of the rotor, the amplitudes and phases are similar to those of TS-waves. However, the growth rates are no longer according to those predicted by linear stability theory for a flat plate flow: As mentioned above, the (smoothed) amplitude keeps growing downstream of the forcing region, whereas it should decay according to Fig.14. The reason for this growth is apparently the high amplitudes of the lower modes, which have an important effect on mode 15 as well.

6.2.7.   Influence of Fundamental Mode

To evaluate the influence of the fundamental mode on the total disturbance flow, the relation between the signal containing all modes and that of mode 1 alone was investigated. Fig.26 shows the total disturbance u', recorded for all x at several timesteps. A closer inspection reveals strong growth of high frequency components (spikes) in the wave troughs of the fundamental mode.

This was further confirmed by comparing the total disturbance flow and the disturbance flow of mode 1 only, as shown in Fig.27. The mode 1 signal was re-computed from the stationary baseflow and from the Fourier coefficients of mode 1. The growth of high frequency components in the mode 1 wave troughs is evident, as is the damping of high frequency components in the mode 1 wave crests. This can also be observed from experimental data (Figs.11, 13).

Although there are quantitative differences between the experimental and numerical data, the qualitative agreement is satisfactory, and the essential features are the same. Therefore one can expect that the receptivity mechanism is the same in both cases, and that the mechanism proposed in the next chapter can explain the questions left open by the experiment.

7. Concept of Receptivity Mechanism

The conclusion is that the high amplitudes of the lowest modes alter (locally in space and time) the stability characteristics of that flow in such a way that the fundamental mode together with the staedy mean flow serve as a new "baseflow" for the instability of the higher modes. The phase velocity of the forcing field is close to that of the most unstable TS waves. All disturbance modes introduced by the forcing have comparable phase speeds (between $0.28\,U_\infty$ and $0.36\,U_\infty$ near the rotor station), but the frequencies and wavelengths of the lowest and highest modes are an order of magnitude apart. Therefore, the low frequency disturbances (mode 1,2,3 ...) can be superimposed on the stationary flow and act as a time-dependend "baseflow" for a high frequency disturbance, say mode 8 or 12. As a consequence, TS waves that "travel" in a wave trough of the low modes experience a more destabilizing "baseflow" and they are therefore more strongly amplified than in a steady flat plate boundary layer. TS waves that "travel" on a wave crest of the low modes are less amplified or even damped.

For all modes, there is a phase shift over y between the freestream and the vertical location of maximum amplitude inside the boundary layer. Therefore, a disturbance that is introduced as a wavecrest at the freestream boundary (or through the rotor rotation in the experiment) experiences a phase shift over y and forms a wavetrough inside the boundary layer that acts as a destabilizing "baseflow" for TS waves. By the same reasoning, a wavetrough in the freestream disturbance leads to a wavecrest inside the boundary layer and thus to a more stabilizing "baseflow". This process is illustrated in Fig.28.

This mechanism can explain the development of the sharp spikes in the boundary layer as it responds to the forcing. The lowest modes are already forced far upstream of the rotor station, but the flat plate baseflow at this Reynolds number is stable for these frequencies. Therefore, their amplitudes inside the boundary layer are highest in the region near the rotor, and they decay downstream, where the forcing amplitudes decrease.

The forcing of the higher (unstable) modes does not set in until much closer to the rotor station, where the amplitudes of the lowest modes are very high. Hence, the higher modes experience a changed baseflow: The low mode wave troughs are more "receptive" to high frequency disturbances than the wave crests. These high frequency disturbances are then strongly amplified when traveling downstream in the low mode wave trough, or damped in a wave crest. The strong spikes in the (barely observable) troughs of mode 1 far downstream are the result of this process.

Because the low mode disturbances are all in phase underneath the rotor, the effect of this mechanism on the higher modes is very strong, as demonstrated by the $u'(t)$ plots in Figs. 10, 12 and 13. The distinct spikes in the low mode wave troughs (see Fig.12) will most likely become turbulent spots further downstream.

Because this process is not symmetric, the RMS amplitudes are higher than those predicted by LST for a stationary baseflow. A low mode wave trough of 1% amplitude results in much stronger amplification than in a steady flow, a wave crest of same amplitude in only moderately less amplification. This can be regarded as

a hysteresis in the amplification mechanism.

Downstream of the rotor, there is a broad spectrum of frequencies with rather high amplitudes present in both experiment and simulation (see Figs. 16,17). Together with the mechanism described above, this leads to a strong, partly nonlinear amplification of those modes that are already past the upper branch of the neutral stability curve (for a flat plate baseflow). These are modes 11–15, with the highest ones (13–15) exhibiting particularly irregular, nonlinear amplitude (y) and phase (y) profiles.

8. Verification of Receptivity Mechanism

8.1. Influence of Forcing Amplitudes

The mechanism proposed here can also explain the difference in the forcing efficiency of 0.48 cm and 0.32 cm rods that was observed by Kendall. The larger rods induce higher forcing amplitudes for all modes, in particular also for the lowest modes. Consequently, the wave troughs in the receptivity region are more distinct, and the higher modes are stronger amplified here than in the case with the smaller rods. This should lead to a higher output/input (o/i) ratio for the larger rods.

To verify this reasoning, two additional test runs were performed. The phases of the forcing functions were the same as in the simulation of the experiment. However, all forcing amplitudes were multiplied by a factor of 2/3 (test case small) and 4/3 (test case big), thus preserving the waveform of the forcing.

One expects that the o/i ratio for the lowest modes (1,2,3) should be roughly the same in all three cases. Their wavelengths and frequencies are not very different from those of mode 1, therefore they are not so strongly affected by the transient change of the baseflow stability characteristics. On the other hand, the amplification rates of the higher modes depend directly on the forcing amplitudes of the lowest modes. Thus, higher forcing amplitudes (test case big) should yield a higher o/i ratio for the higher modes than the reference case, whereas lower forcing amplitudes (test case small) should yield a lower o/i ratio.

The o/i ratios for all three cases are plotted in Fig.29. Here, "Lauf 1" refers to the reference case, "big" to the test case with forcing amplitudes multiplied by 4/3, and "small" to the test case with forcing amplitudes multiplied by 2/3. The "input" amplitudes are those recorded at the point $(n = 82, m = 51)$ underneath the rotor, and the "output" amplitudes are recorded at the point $(n = 122, m = 9)$. These locations correspond to the ones used by Kendall in the evaluation of the experimental data. For comparison, the experimental data are plotted in Fig.30 (Kendall 1987, Fig.15). It should be noted here that Kendall used the nondimensionalized disturbance velocity u'/U_∞ as output and the nondimensionalized disturbance pressure p'/q_0 as input , where $q_0 = \rho U_\infty^2/2$. In the evaluation of the numerical data, the nondimensionalized disturbance velocity u'/U_∞ was used. Therefore, a o/i ratio of 80 in the numerical data (Fig.29) corresponds to a o/i ratio of 40 in the experimental data (Fig.30).

The output/input ratios of the three cases are as expected. The stronger low mode forcing results in stronger amplification of the TS waves, and the maximum o/i ratio is shifted to a higher mode. On the other hand, the lower modes do not exhibit very different o/i ratios. This agrees well with the experimental data. However, since the waveforms of the 0.32 cm and 0.48 cm forcing in the experiment were different, one can only qualitatively compare the two curves in Fig.30. A quantitative comparison is possible in Fig.29 (numerical data), because the relative waveforms were the same in all three cases. It is one of the advantages of numerical simulations that the "input" can easily be controlled, whereas this is extremely difficult to do in physical experiments.

The fact that the o/i ratios of the reference case (Lauf 1) are smaller than those of the experiment is due to the smaller output amplitudes. The reason for this are the weaker background turbulence in the simulation and the weaker forcing of mode 1, as was discussed chapter 6.

8.2.   Comparison of Navier-Stokes Results and Linear Stability Theory

If the mechanism described above is indeed relevant, then the qualitative behavior should be similar in a model where only two modes are used. This idea was tested in another numerical calculation. The parameters for the computer run were the same as in the "test case small" run of the previous section to ensure that the amplitudes would not be too high for linear growth. But instead of a broad frequency spectrum, the forcing function consisted of only two frequencies: Mode 1 was to force the high-amplitude, low-frequency disturbance,and mode 8 was to induce an unstable TS wave. Since the amplitude of mode 1 was much higher than the amplitude of mode 8 in the center of the forcing region, the feedback of mode 8 on the amplification of mode 1 is expected to be negligible. Indeed, it turned out that the amplitude of mode 1 at the aft limit of the forcing is somewhat smaller than that in the simulation with all modes present. This confirms the assumption that nonlinear effects played a certain role in the amplification downstream of the rotor.

The forcing signal u' at x=0.66 m is plotted in Fig.31 for two different distances from the wall: First at the freestream boundary ($m = 121$) and second at a distance of about two boundary layer thicknesses ($m = 51$). Here one can clearly observe the mode 1 signal and superimposed on it mode 8. The disturbance signal u' inside the boundary layer at a location far downstream (x=1.14 m) is plotted in Fig.32.

The modulation of the mode 8 amplitude over one period of the fundamental is evident in Fig.32. In order to evaluate the effect of the mode 1 fluctuation on the amplification of mode 8, the maximum amplitude was divided by the minimum amplitude (of mode 8). The amplification ratio is

$$\left(\frac{\text{max.ampl}}{\text{min.ampl}}\right)_{\text{N-St}} = 1.49$$

For comparison of this result with the amplitude growth predicted by linear stability theory (LST), the mean flow and mode 1 were combined to form the time-dependend "baseflow" for the TS waves. The so obtained velocity profiles were used as the baseflow-profiles in the Orr-Sommerfeld equation. This equation was then solved to compute the growth rates of normal modes of frequency $F8$ at subsequent x-locations, following the path of a TS wave traveling downstream in either a wave trough or a wave crest. The differences between the stationary flow profiles and the "baseflow" profiles used for the LST computation are plotted in Fig.33 a,b . The velocity profiles that lead to maximum amplification of a TS-wave are shown in Fig.33a: A wave trough over most of the integration domain is characteristic for that case. Because the phase speed of mode 8 is higher than that of mode 1, TS

waves that are at first amplified in a low mode wave trough travel a little faster than that trough. After some time, they reach the next wave crest, where the growth rates are smaller. This dispersion effect can be seen in Fig.33 a: The velocity profile at the downstream end of the integration domain at x=1.14 m has a wave crest inside the boundary layer, hence a mode 8 disturbance should be less amplified at that location than in the case of a steady baseflow. This agrees with the observation of the spike growth in Fig.27. On the other hand, TS waves that are at first damped in a wavecrest are amplified when they reach the next wave trough. The velocity profiles for least amplification are shown in Fig.33b .

The growth rates $-\alpha_i$ for four cases are plotted in Fig.34, where α_i is nondimensionalized by multiplication with $L=0.66$ m:

I.   maximum amplification, computed from LST with destabilizing "baseflow".
II.   maximum amplification, computed from LST with stabilizing "baseflow".
III.   amplification in steady mean flow, computed from LST with steady boundary layer baseflow.
IV.   average amplification, obtained from the Fourier analysis of the Navier-Stokes computation ($\sim$ Lauf 2).

It can be observed that the average amplification in the Navier-Stokes computation is somewhat higher than that predicted by LST for a steady baseflow, this confirms the notion of the hysteresis-like mechanism. Also, due to the dispersion mentioned above, the amplification rate of case I is lower than that of case II at the end of the observed domain.

To compare the amplification rate predicted by linear stability theory with that from the Navier-Stokes simulation, the amplitude ratio (maximum amplification / minimum amplification) was evaluated. It is

$$\left(\frac{\text{max.ampl}}{\text{min.ampl}}\right)_{\text{LST}} = 1.58 \, ,$$

which is about 6% higher than the value obtained in the Navier-Stokes calculation. This is rather accurate for an integration domain of more than 14 TS-wavelengths, considering that the disturbances are not simply amplified in the Navier-Stokes calculation, but first introduced from the freestream. It appears that the transient change of the receptivity coefficient in wave troughs and wave crests is about proportional to the transient change of the instability amplification. This assumption needs to be further investigated by analytical (or semi-analytical) means.

One should also note that the amplification rates obtained from linear stability theory are computed with the assumption of parallel baseflow at each streamwise location. Thus, any gradient of the baseflow velocity in streamwise direction is neglected. The fact that there is a very good agreement between these results and the results of the Navier Stokes simulation suggests that the transient change in the amplification rates is mostly due to the variation of the "baseflow" velocity profiles in normal direction, and that the gradient of the "baseflow" velocity in streamwise direction is considerably less important.

The results of this numerical experiment confirm the concept of the receptivity mechanism described in chapter 7.

9. Conclusions

The numerical simulation led to a new model for this receptivity mechanism. It was demonstrated how low-frequency (LF) freestream perturbations with high amplitudes can affect both the initial amplitudes of high-frequency (HF) disturbances within the boundary layer and the subsequent amplification of these disturbances as they travel downstream.

The essential feature of this mechanism is the large difference in length and time scales between the low frequency disturbances and the amplified TS waves. When the LF disturbances are superimposed on the steady boundary layer flow, they alter (locally in space and time) its stability characteristics. Steady flow and LF disturbances together form a new, time dependent "baseflow" for disturbances with higher frequencies. First, in a wavetrough of the LF disturbances the flow is more "receptive" to disturbances with higher frequencies when compared to the steady mean flow, i.e. a given HF freestream perturbation generates a HF disturbance (a TS wave) with a higher initial amplitude in the boundary layer. Second, the TS wave is more strongly amplified as it travels downstream, because the "baseflow" in the LF wavetrough is more unstable than the steady mean flow. Similarly, the "baseflow" formed by a LF wavecrest is less "receptive" and more stable for TS-waves.

There is no reason for this process to be restricted to freestream disturbance fields with a phase speed close to that of the most unstable TS waves. If the wavelength and frequency are sufficiently different (very low frequency disturbance vs. TS waves), and if the low-frequency forcing is strong enough (forcing extended over a large domain, high forcing amplitudes), the described mechanism may well be important for receptivity to unsteady pressure fields that travel at the freestream speed U_∞. Possible examples are buffeted boundary layers, or the "breathing mode" of boundary layers induced by grids in a windtunnel (Kendall, 1985): There are certainly non-negligible 3-D effects present, but the high-amplitude, low frequency disturbances reported by Klebanoff (1971) and Kendall (1985) should also play an important role in the amplification of TS waves which can be ascribed to the mechanism presented in this report. However, further experiments, both physical and numerical, need to be carried out to support these conjectures.

References

Fasel, H. (1976), "Investigation of the Stability of Boundary Layers by a Finite Difference Model of the Navier-Stokes Equations," *J. Fluid Mech.*, Vol. 62, pp. 249-261

Fasel, H. (1979), "Numerische Simulation Inkompressibler Viskoser Strömungen," *Habilitationsschrift*, Universität Stuttgart

Gruber, K. (1987), " Numerische Untersuchungen zum Problem der Grenzschichtablösung," *Dissertation*, Universität Stuttgart

Kendall, J.M. (1985), "Experimental Study of Disturbances Produced in a Pre-Transitional Laminar Boundary Layer by Weak Freestream Turbulence," *AIAA Paper* 85-1695

Kendall, J.M. (1987), "Experimental Study of Laminar Boundary Layer Receptivity to a Traveling Pressure Field," *AIAA Paper* 87-1257

Kendall, J.M. (1987,I), private communication

Klebanoff, P. (1971), "Effect of Freestream Turbulence on the Laminar Boundary Layer (Abstract)," *Bull. Am. Phys. Soc.*, Vol. 10 No. 11, p. 1323, Nov. 1971

Kerschen, E. (1989), "Boundary Layer Receptivity," *AIAA Paper* 89-1109

Morkovin, M.V. (1988), "Recent Insights into Instability and Transition to Turbulence in Open-Flow Systems," *ICASE-Report* No. 88-44

Nishioka, M., and Morkovin, M.V. (1986), "Boundary-Layer Receptivity to Unsteady Pressure Gradients: Experiments and Overview," *J. Fluid Mech.*, Vol. 171, pp. 219-261

Rist, U. (1989), "Numerische Untersuchung der räumlichen dreidimensionalen Störungsentwicklung beim Grenzschichtumschlag," *PhD Thesis*, Universität Stuttgart

Appendix A: Parameters for the Simulation

Experimental Parameters

The parameters of the particular experimental configuration simulated numerically were the following:

freestream speed $U_\infty = 11.6 \text{ m/s}$

Reynolds number $Re = 4.761 \times 10^5$ (based on $L = x_c = 0.66 \text{ m}$)

diameter of rods $\emptyset_r = 0.48 \text{ cm}$

frequency of mode 1 $F_1 = 0.0685$

phase speed of forcing $u_s = 0.33 \times U_\infty$

where:

$$F_n = \frac{\nu \beta_n}{U_\infty^2} \times 10^4 \text{ dimensionless frequency}$$

β_n : circular frequency in rad/s

ν : dynamic viscosity in m^2/s

Mode 1 through mode 15 denote the components of the Fourier transform of the disturbance (both forcing and response): Due to the forcing by revolving rods, the flow is periodic with period $T_1 = 2\pi/\beta_1$.

Numerical Parameters

The parameters used for the numerical simulation were the following:

$$\hat{x}_0 = 160 \text{ mm}$$
$$\hat{x}_{we} = 1182 \text{ mm} \qquad N_E = 499$$
$$\hat{x}_e = 1595 \text{ mm} \qquad N = 700$$
$$\hat{Y} = 19.46 \text{ mm} \qquad M = 121$$
$$\Delta \hat{t} = 4.2819 \times 10^{-5} \text{ s} \qquad T_1 = 2560 \, \Delta \hat{t}$$

where:

T_1 : period of mode 1

Only the values at every third x-gridline up to N_E were stored on tape at every 10th timestep. Thus, the stored data cover a $(M \times N) = (121 \times 167)$ grid, and they are periodic over 256 timesteps. The gridlines referred to in chapters 6 – 8 are those of the (121×167) grid.

Appendix B: Tables

Table 1: Forcing Coefficients				
Mode	b_l [m^{-2}]	ψ_l	re(c_l)	im(c_l)
1	40.	1.03	111.17	-212.05
2	56.	1.04	92.09	-102.58
3	64.	1.06	76.88	-48.23
4	84.	1.13	59.15	-20.99
5	159.	1.32	44.00	-9.20
6	167.	1.48	30.25	-4.19
7	296.	1.89	21.10	-0.90
8	298.	2.24	13.60	-0.46
9	302.	2.73	9.19	0.34
10	349.	3.52	5.95	0.42
11	375.	4.50	3.87	0.14
12	400.	5.86	2.58	0.14
13	425.	8.04	1.46	0.22
14	450.	10.11	1.01	-0.04
15	475.	15.53	0.63	0.16

Table 2: Forcing Amplitudes Experiment	
Mode	u'/U_∞
1	0.25×10^{-2}
2	0.14×10^{-2}
3	0.94×10^{-3}
4	0.65×10^{-3}
5	0.46×10^{-3}
6	0.32×10^{-3}
7	0.22×10^{-3}
8	0.14×10^{-3}
9	0.95×10^{-4}
10	0.62×10^{-4}
11	0.40×10^{-4}
12	0.27×10^{-4}
13	0.15×10^{-4}
14	0.10×10^{-4}
15	0.67×10^{-5}

Table 3: Forcing Amplitudes Simulation	
Mode	u'
1	0.24×10^{-2}
2	0.14×10^{-2}
3	0.93×10^{-3}
4	0.64×10^{-3}
5	0.45×10^{-3}
6	0.30×10^{-3}
7	0.20×10^{-3}
8	0.13×10^{-3}
9	0.83×10^{-4}
10	0.54×10^{-4}
11	0.35×10^{-4}
12	0.23×10^{-4}
13	0.13×10^{-4}
14	0.90×10^{-5}
15	0.67×10^{-5}

Table 4: Output Amplitudes Experiment	
Mode	u'/U_∞
1	0.78×10^{-2}
2	0.32×10^{-2}
3	0.39×10^{-2}
4	0.45×10^{-2}
5	0.52×10^{-2}
6	0.59×10^{-2}
7	0.63×10^{-2}
8	0.61×10^{-2}
9	0.54×10^{-2}
10	0.43×10^{-2}
11	0.30×10^{-2}
12	0.17×10^{-2}
13	*n.a.*
14	*n.a.*
15	*n.a.*

Table 5: Output Amplitudes Simulation	
Mode	u'
1	0.66×10^{-2}
2	0.28×10^{-2}
3	0.26×10^{-2}
4	0.32×10^{-2}
5	0.39×10^{-2}
6	0.46×10^{-2}
7	0.46×10^{-2}
8	0.43×10^{-2}
9	0.37×10^{-2}
10	0.27×10^{-2}
11	0.17×10^{-2}
12	0.90×10^{-3}
13	0.32×10^{-3}
14	0.11×10^{-3}
15	0.18×10^{-3}

Appendix C: The Interference Between Two Waves with Same Frequency and Different Wavenumbers

Let

$$f = \psi_f(x,y) \exp i(\alpha_f x - \beta t)$$
$$g = \psi_g(x,y) \exp i(\alpha_g x - \beta t)$$

be two spatially developing waves with the same frequency. ψ_f and ψ_g are the (complex) amplitude distribution functions, α_f and α_g are the complex wavenumbers, and β is the real circular frequency:

$$\psi_f = \psi_{Re,f} + \psi_{Im,f}$$
$$\psi_g = \psi_{Re,g} + \psi_{Im,g}$$
$$\alpha_f = \alpha_{Re,f} + \alpha_{Im,f}$$
$$\alpha_g = \alpha_{Re,g} + \alpha_{Im,g}$$

where

$$\alpha_{Re,f}\, c_f = \beta$$
$$\alpha_{Re,g}\, c_g = \beta$$

c_f, c_g are the phase speeds of the waves. The subscript $_{Re}$ denotes the real part and the subscript $_{Im}$ denotes the imaginary part of a complex number.

The time average of the product $f \cdot g$ can then be expressed through

$$\overline{f \cdot g} = \frac{1}{2}\, \mathrm{Re}\{\, \psi_f\, \psi^*_g\, \exp i(\alpha_{Re,f} - \alpha_{Re,g})x \,\}\, \exp -(\alpha_{Im,f} + \alpha_{Im,g})x$$

where the superscript * denotes the complex conjugate (Nishioka and Morkovin,1986). The amplitude of the product grows with $\exp -(\alpha_{Im,f} + \alpha_{Im,g})x$ and oscillates around this mean value with $\exp i(\alpha_{Re,f} - \alpha_{Re,g})x$. Note that if both waves have the same phase speed (and thus the same real part of the wavenumber), there is no oscillation at all. If the phase speed of one of the waves, say of f, is infinite (and the wavenumber $\alpha_{Re,f}$ is zero), then the average amplitude oscillates with the wavelength of the other wave $\alpha_{Re,g}$.

As an example, consider the modulation of the amplitude of mode 15 in the present work (Figs.15, 16): The frequency is $\beta_{15} = 858.75$ rad/s. The wavenumber of a TS-wave is roughly $\alpha_{Re,TS} = 194$ 1/m, and the wavenumber of the Stokes-type wave is about $\alpha_{Re,St} = 224$ 1/m. The difference is $\alpha_{Re,St} - \alpha_{Re,TS} = 30$ 1/m, that corresponds to an oscillation wavelength of about 0.2 m. This is approximately the distance between relative maxima in the amplitude curve of mode 15 in Fig.16.

Figures
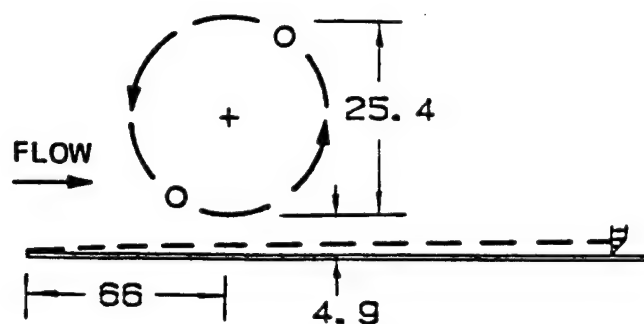
Fig.1. Test configuration showing relation of rotor to boundary layer plate. Dimensions in cm.
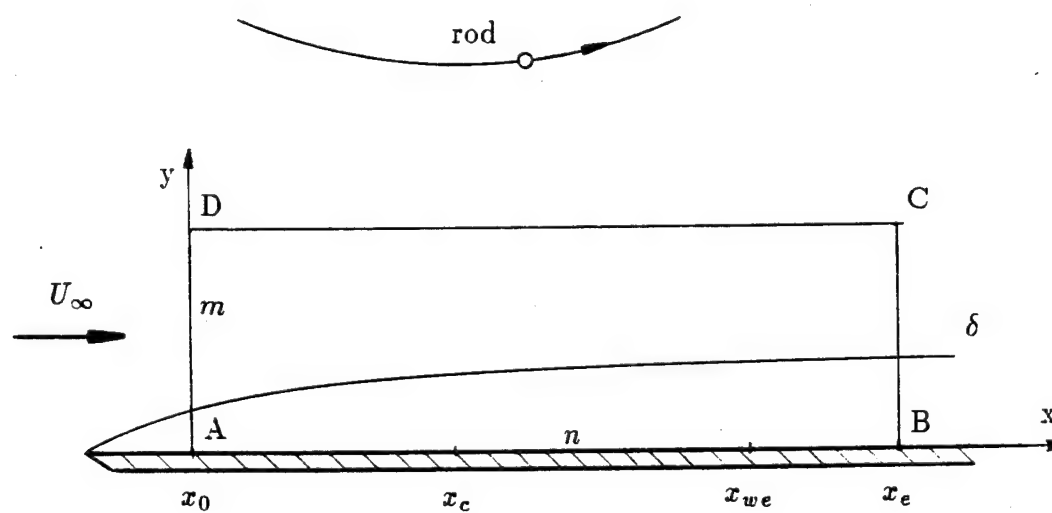
Fig.2. Integration domain for the numerical simulation.
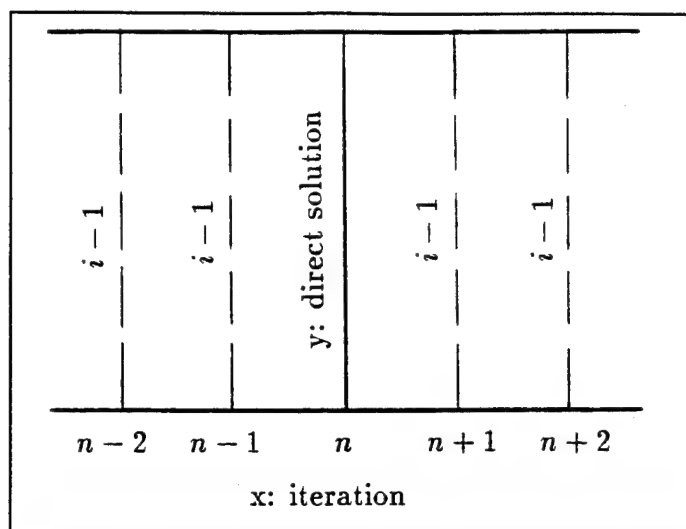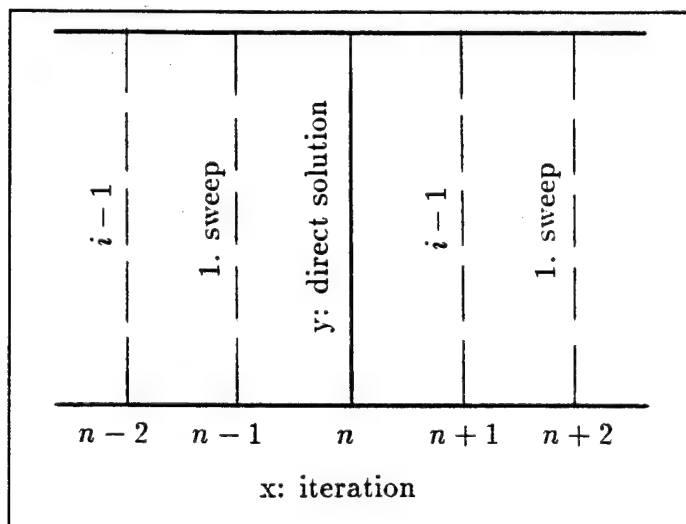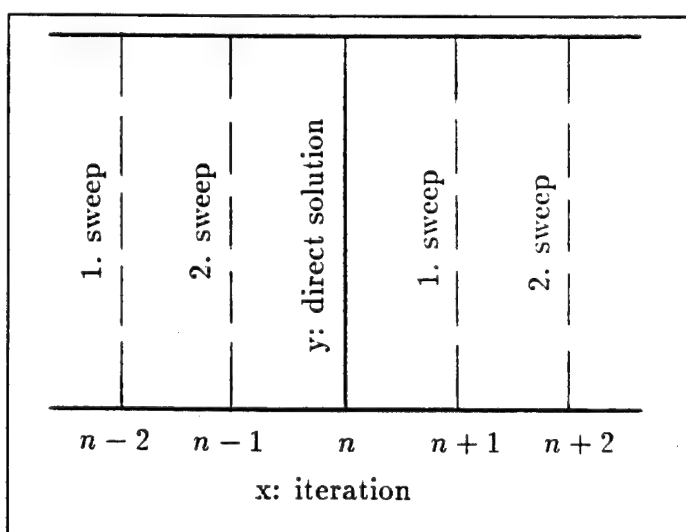
Fig.3 "Zebra" line iteration to solve the Poisson equation for v
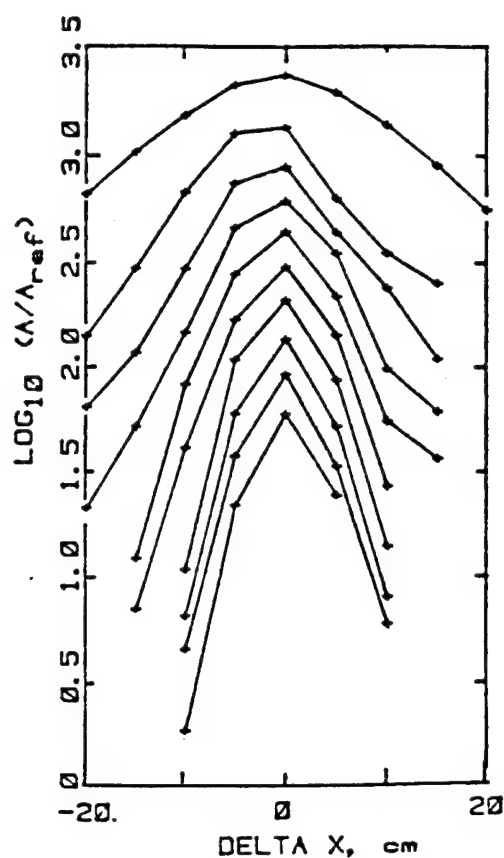
Fig.4. Experiment: Fourier amplitudes of inferred pressure at layer edge, reference is arbitrary. Rotor axis at 0.66 m, measurements at 5.08 cm increments upstream and downstream of axis.
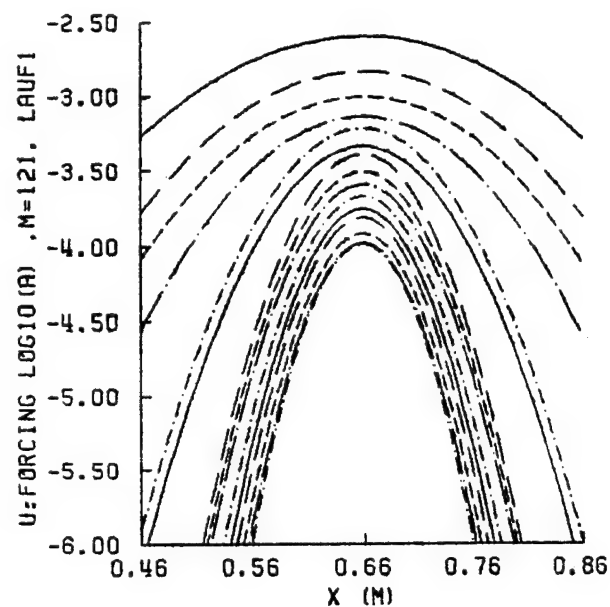
Fig.5. Numerical simulation: Fourier amplitudes of disturbance velocity u' at the freestream boundary ($m = 121$). Rotor axis at $n = 82$ (x=0.66 m).
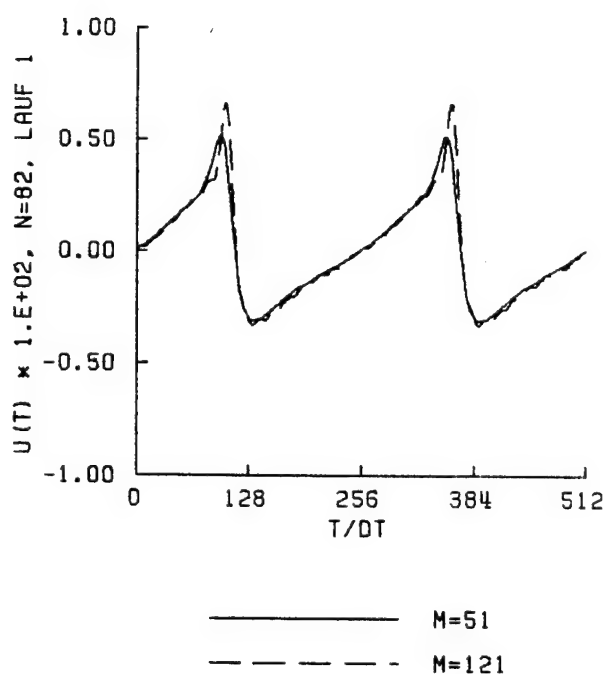
Fig.6. Time signal of the forcing at $n = 82$ (x=0.66 m). Disturbance velocity u' plotted over two periods. $m = 121$ is at the freestream boundary, $m = 51$ is at about two boundary layer thicknesses.

0.359E-01

-0.549E-01

U-VELOCITY, LAUF 1

TIME LEVEL =   1

0.359E-01

-0.549E-01

U-VELOCITY, LAUF 1

TIME LEVEL =   33

Fig.7. u' disturbance velocity over (x,y). Mean flow direction left to right, streamwise coordinate x.

0.359E-01

-0.549E-01

U-VELOCITY, LAUF 1
TIME LEVEL =   65

0.359E-01
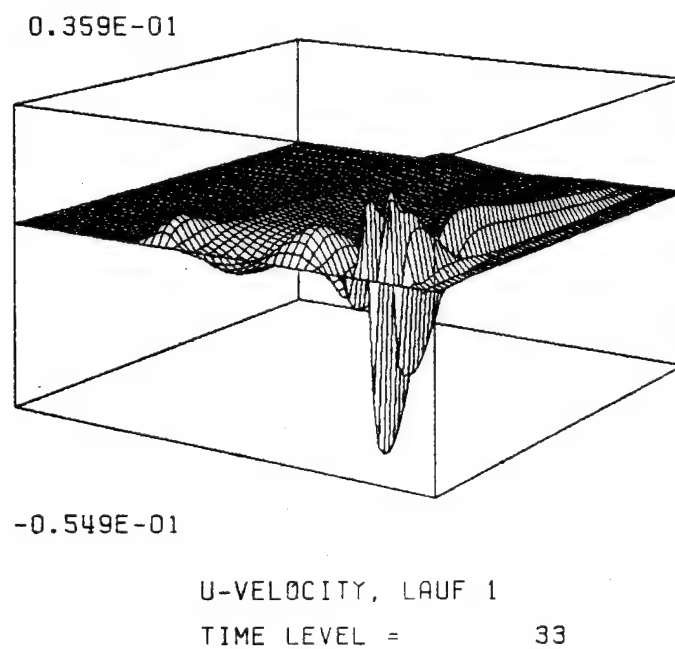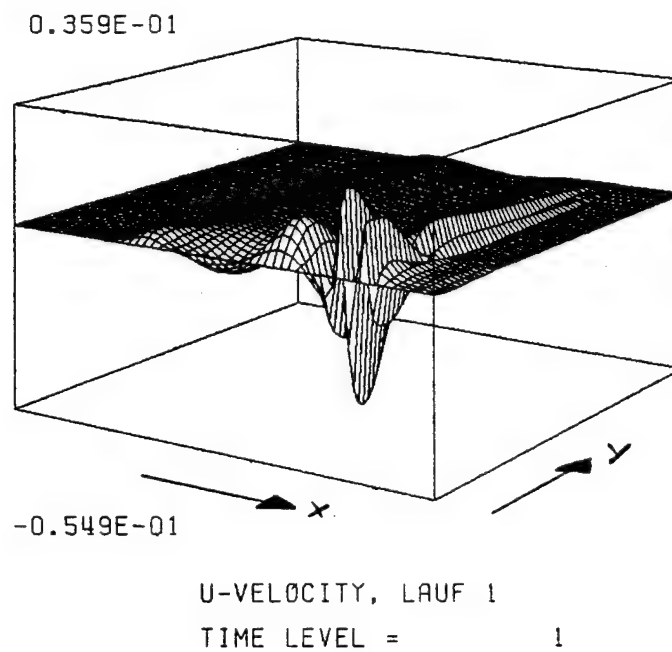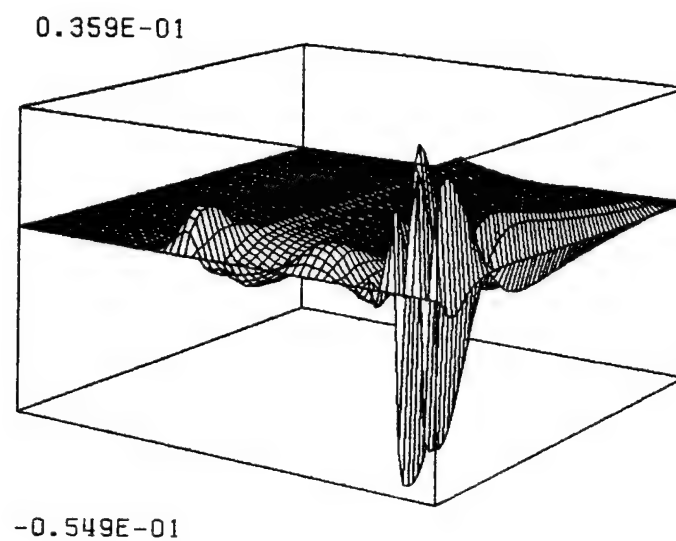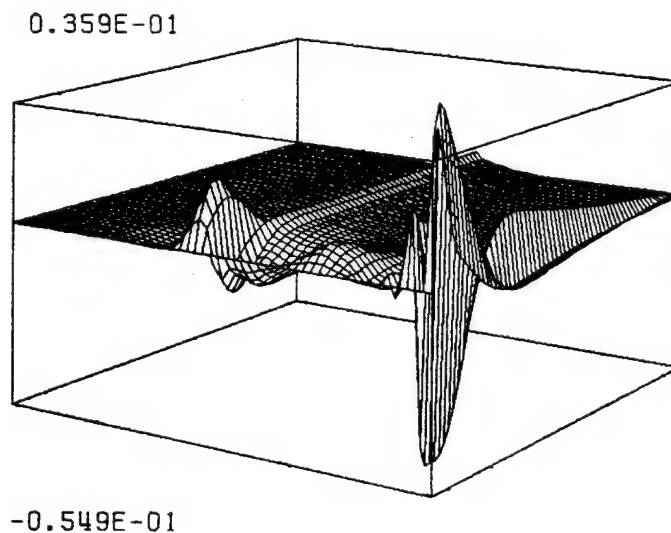
-0.549E-01

U-VELOCITY, LAUF 1
TIME LEVEL =   97

Fig.7. continued

0.359E-01

-0.549E-01

U-VELOCITY, LAUF 1
TIME LEVEL =   129

0.359E-01
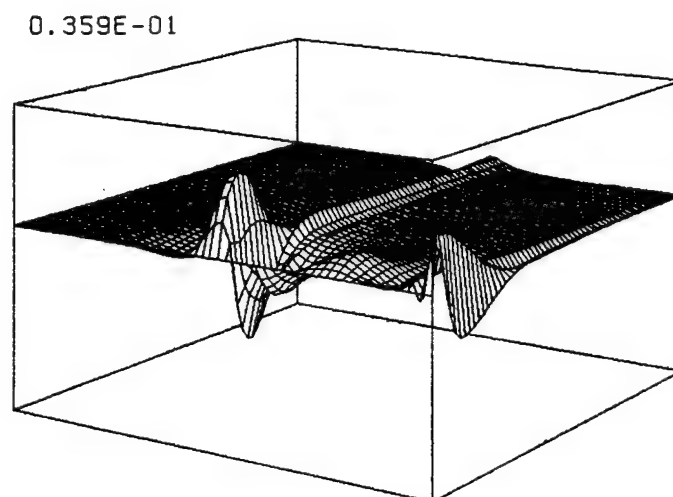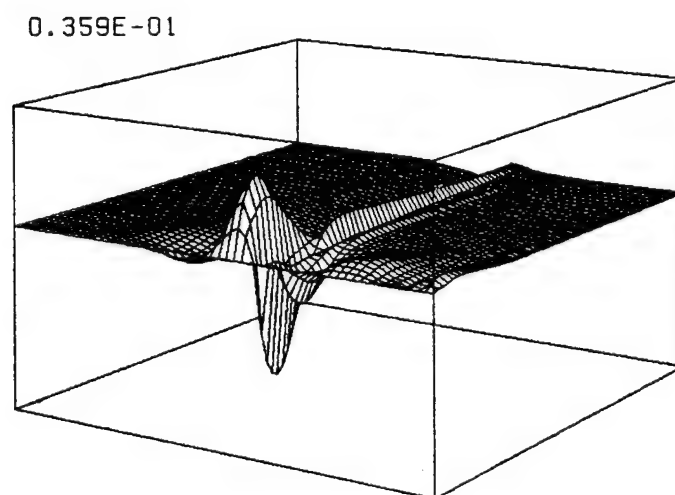
-0.549E-01

U-VELOCITY, LAUF 1
TIME LEVEL =   161

Fig.7. continued

0.359E-01

-0.549E-01

U-VELOCITY, LAUF 1
TIME LEVEL =   193

0.359E-01

-0.549E-01
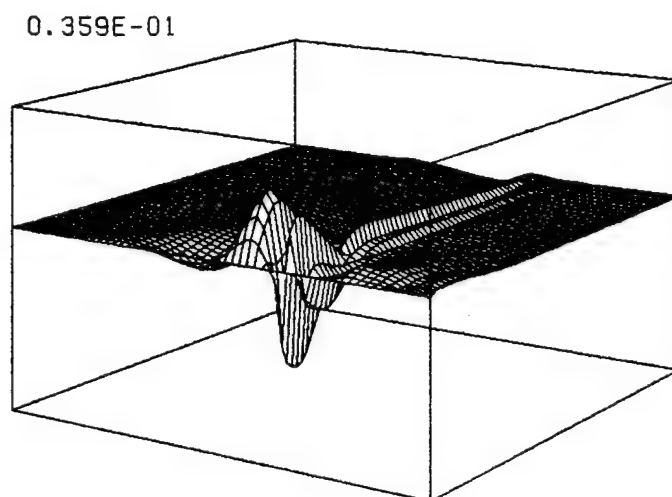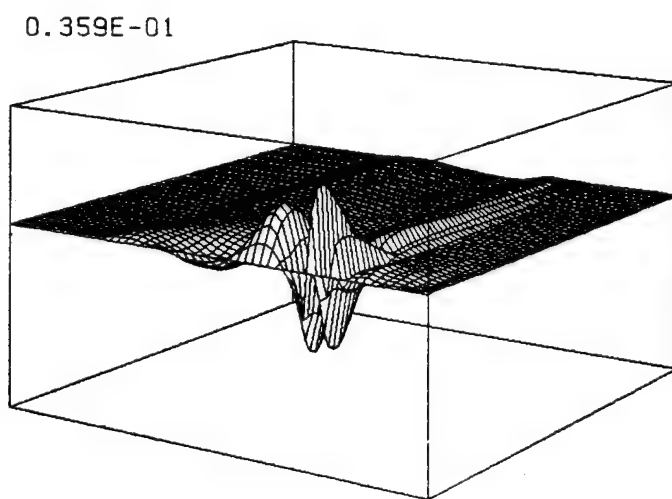
U-VELOCITY, LAUF 1
TIME LEVEL =   225

Fig.7. continued

0.763E+01

-0.109E+02

V-VELOCITY, LAUF 1
TIME LEVEL =   1

0.763E+01

-0.109E+02

V-VELOCITY, LAUF 1
TIME LEVEL =   33
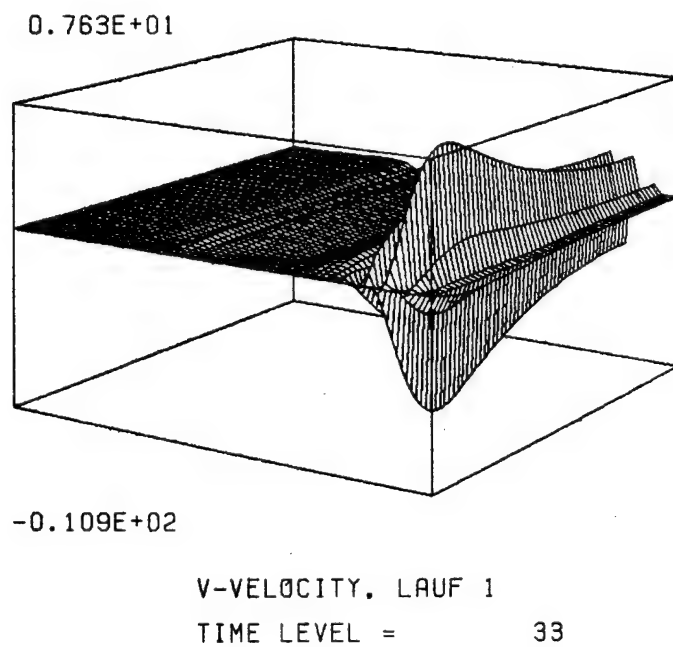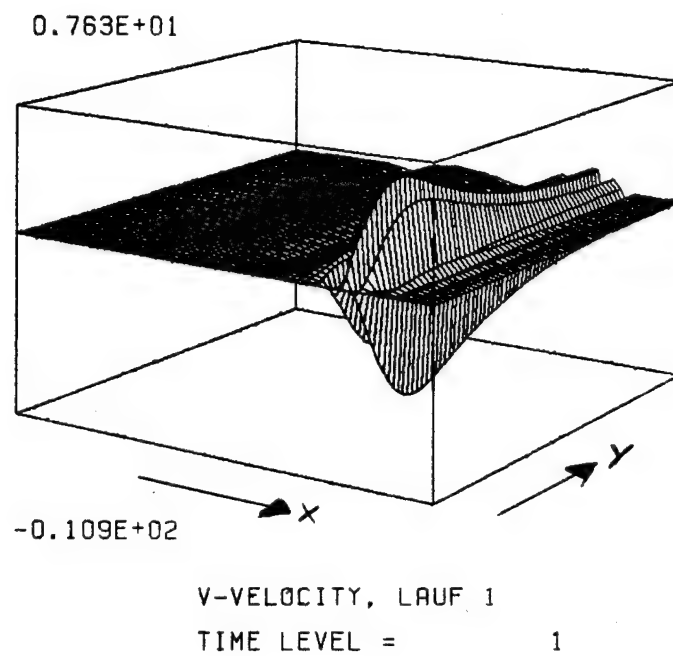
Fig.8. v' disturbance velocity over (x,y). Mean flow direction left to right, streamwise coordinate x.
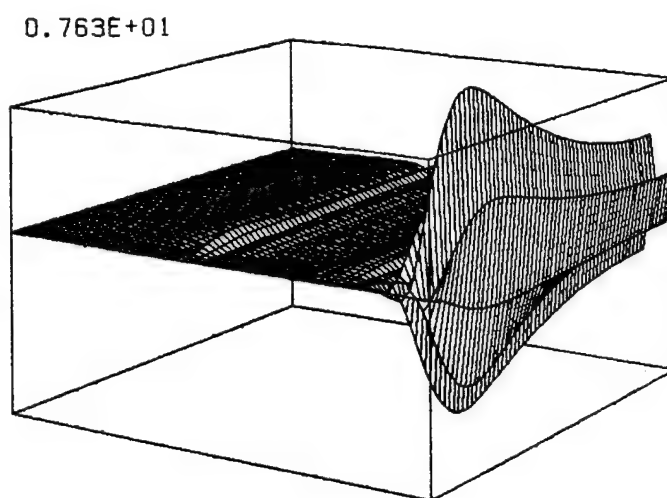
0.763E+01

-0.109E+02

V-VELOCITY, LAUF 1
TIME LEVEL =   65
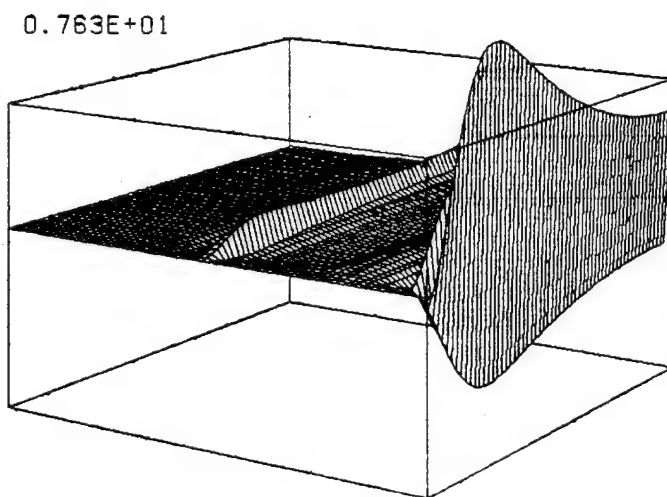
0.763E+01

-0.109E+02

V-VELOCITY, LAUF 1
TIME LEVEL =   97

Fig.8. continued

0.763E+01
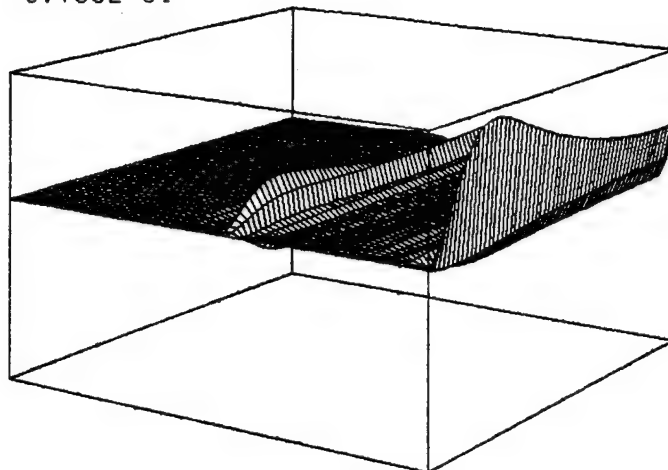
−0.109E+02

V−VELOCITY, LAUF 1
TIME LEVEL =   129

0.763E+01
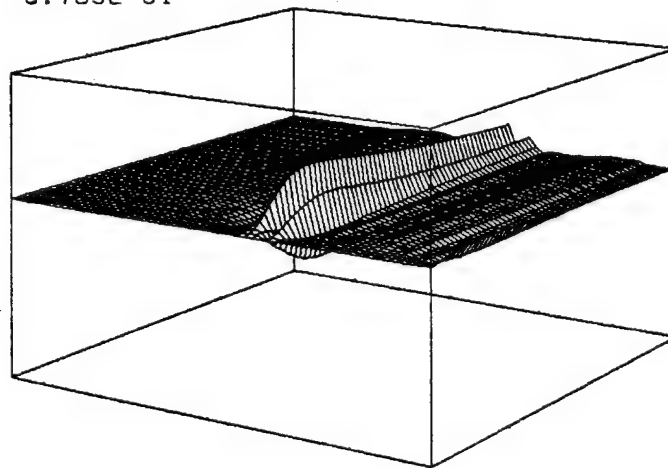
−0.109E+02

V−VELOCITY, LAUF 1
TIME LEVEL =   161

Fig.8. continued

0.763E+01

-0.109E+02

V-VELOCITY, LAUF 1
TIME LEVEL =   193

0.763E+01

-0.109E+02
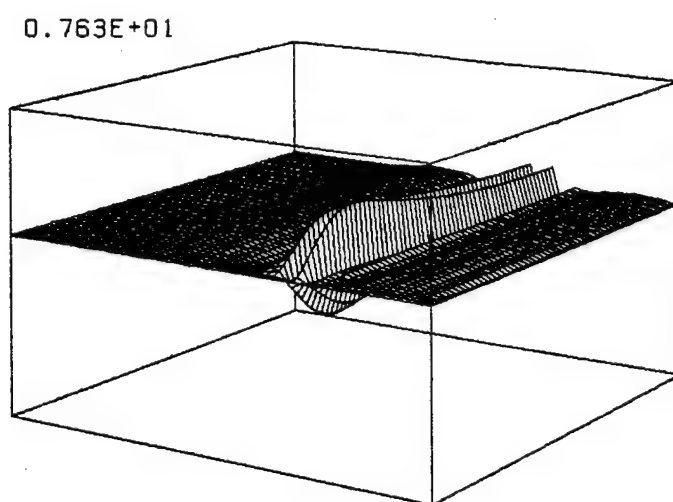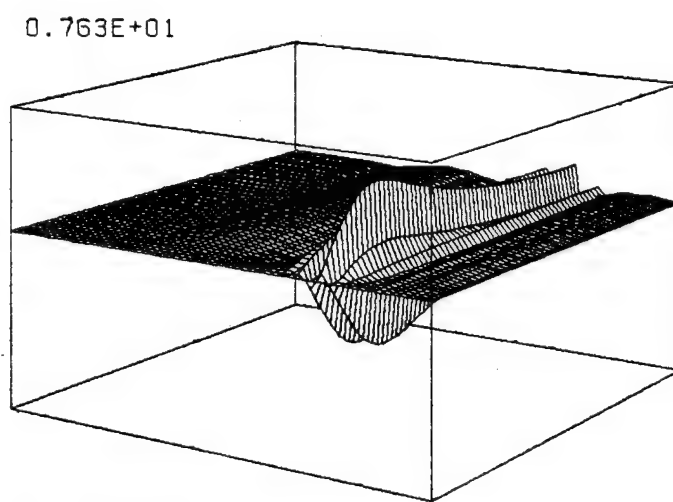
V-VELOCITY, LAUF 1
TIME LEVEL =   225

Fig.8. continued

0.141E+00

-0.843E-01 X Y

VORTICITY, LAUF 1
TIME LEVEL =   1

0.141E+00

-0.843E-01

VORTICITY, LAUF 1
TIME LEVEL =   33
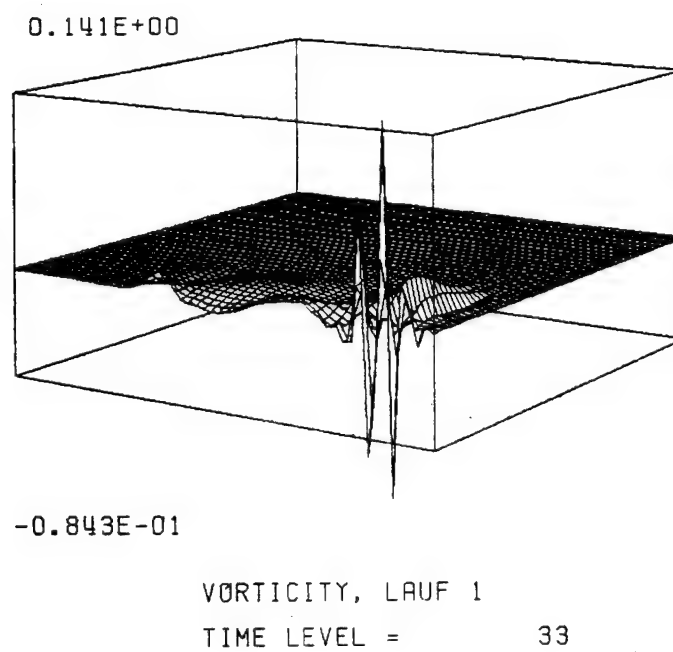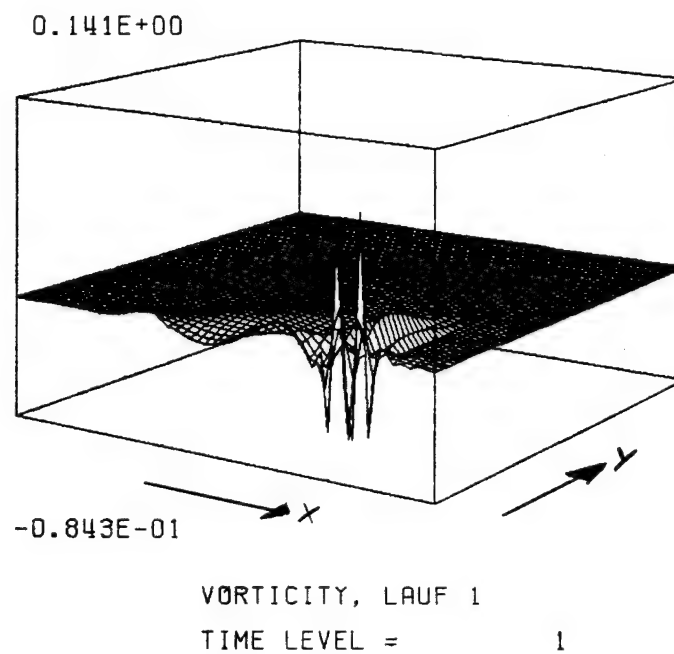
Fig.9. ω' disturbance vorticity over (x,y). Mean flow direction left
to right, streamwise coordinate x.

0.141E+00

-0.843E-01

VORTICITY, LAUF 1
TIME LEVEL =   65

0.141E+00
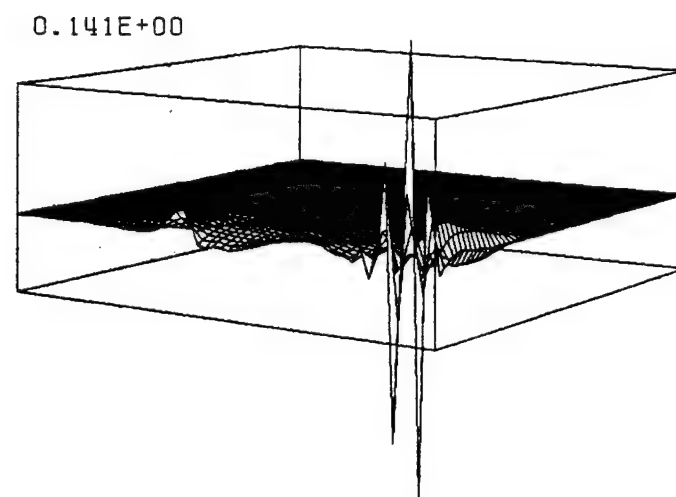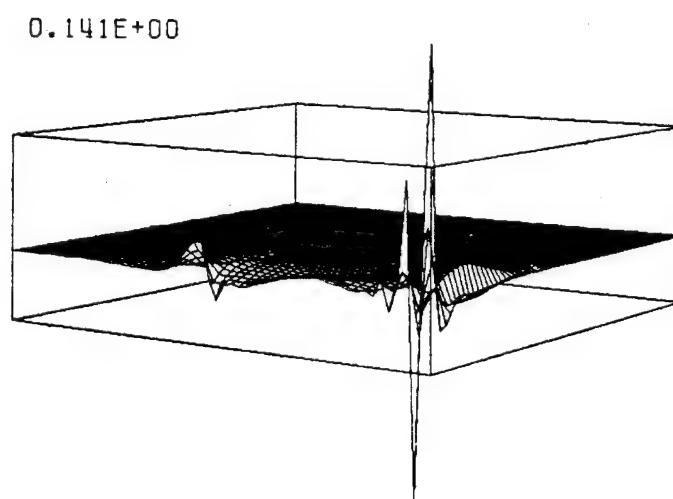
-0.843E-01

VORTICITY, LAUF 1
TIME LEVEL =   97

Fig.9. continued

0.141E+00

-0.843E-01

VORTICITY, LAUF 1
TIME LEVEL =   129

0.141E+00
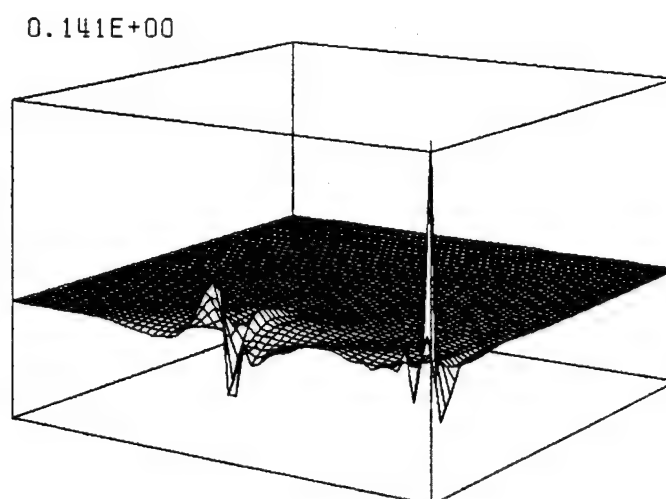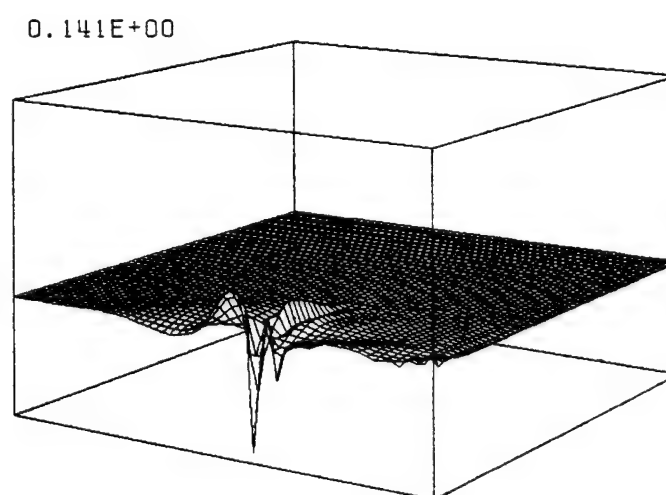
-0.843E-01

VORTICITY, LAUF 1
TIME LEVEL =   161

Fig.9. continued

0.141E+00

-0.843E-01

VORTICITY, LAUF 1
TIME LEVEL =   193

0.141E+00

-0.843E-01

VORTICITY, LAUF 1
TIME LEVEL =   225
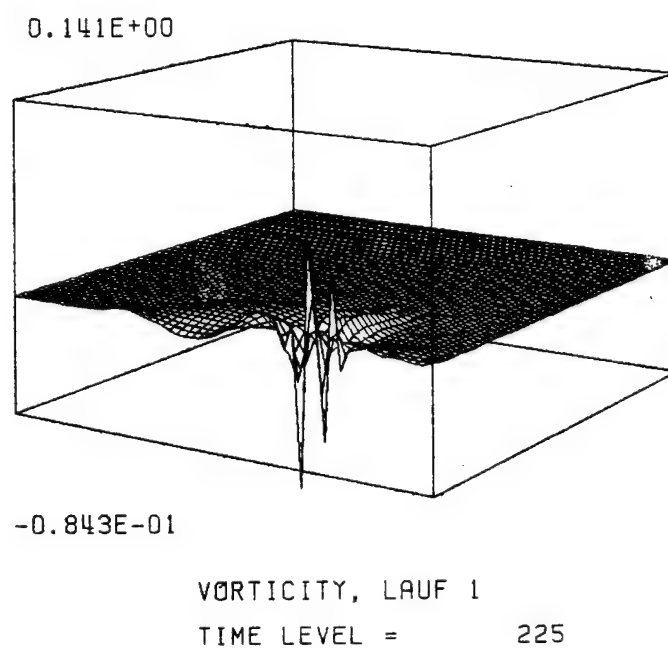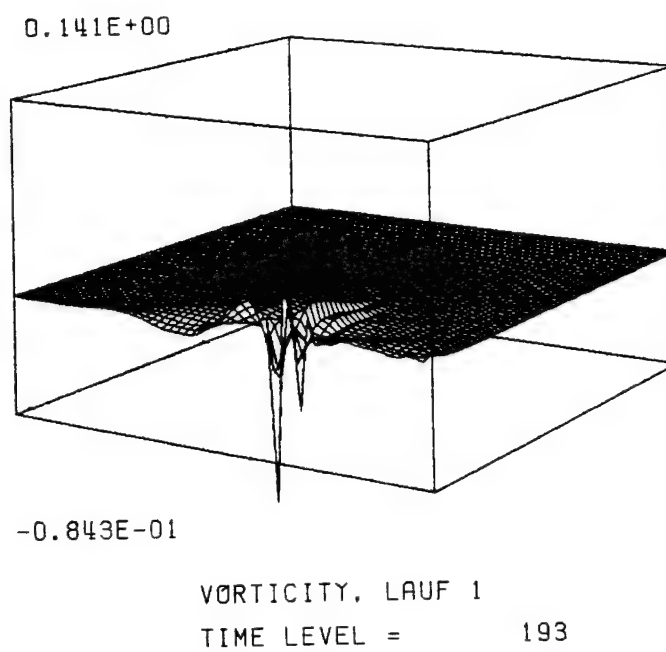
Fig.9. continued
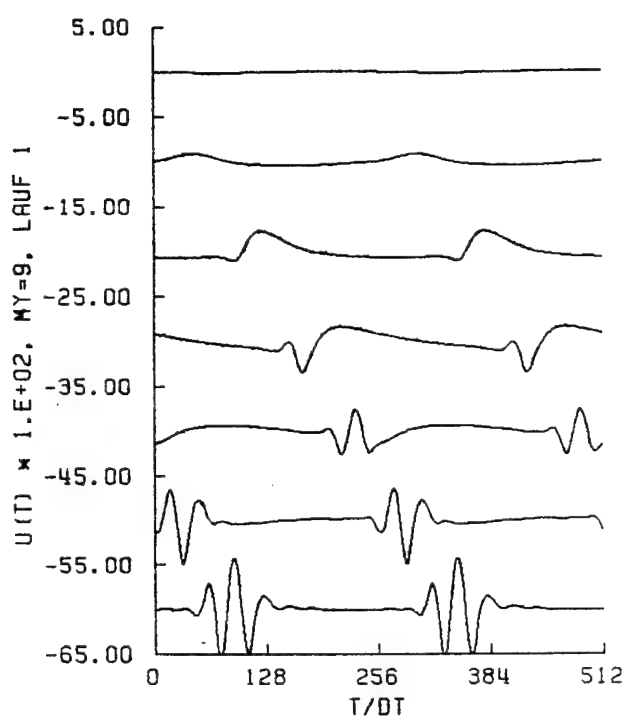
Fig.10. Numerical simulation: Streamwise development of induced TS waves. $u'(t)$ observed over two periods near vertical location of maximum fluctuation. First station (top) at $n = 42$ (x=0.41 m), x-increments are 20 gridlines (12.3 cm). Rotor station is at 0.66 m (third station). Vertical offset between successive baselines corresponds to $u'/U_\infty = 10\%$.
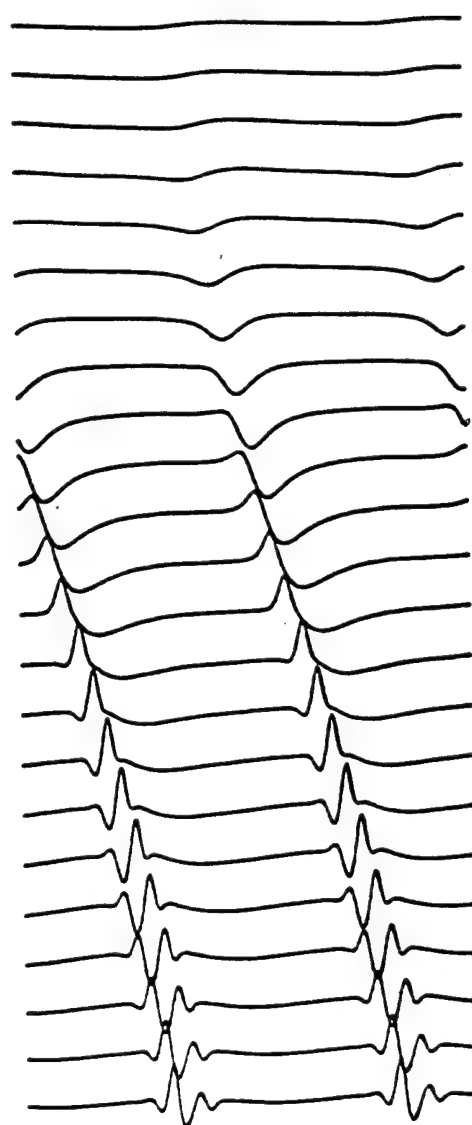
Fig.11. Experiment: Streamwise development of induced TS waves. Observed near vertical location of peak response. First station (top curve) is 0.46 m; increments are 2.54 cm except last is 1.5 cm. Rotor at 0.66 m (ninth station). Vertical offset between successive baselines corresponds to $u'/U_\infty = 0.07$, approximately. Velocity increases upward.

Note: Each curve in this figure is to be reverted upside down for comparison.
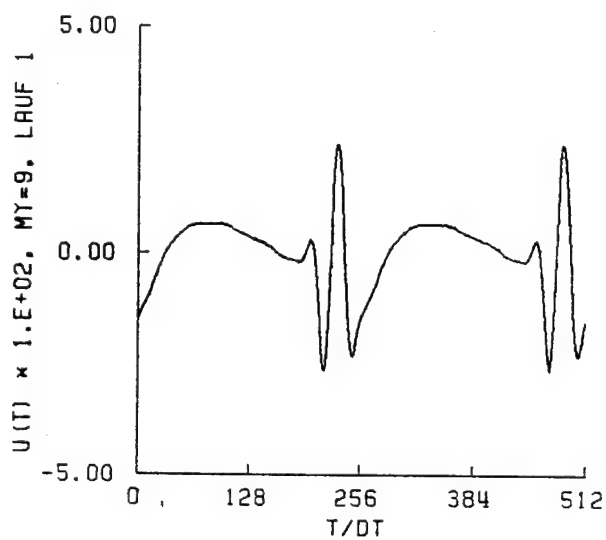
Fig.12. Numerical simulation: Time signal u'(t) observed at $n=122$ (x=0.91 m) near vertical location of maximum fluctuation.
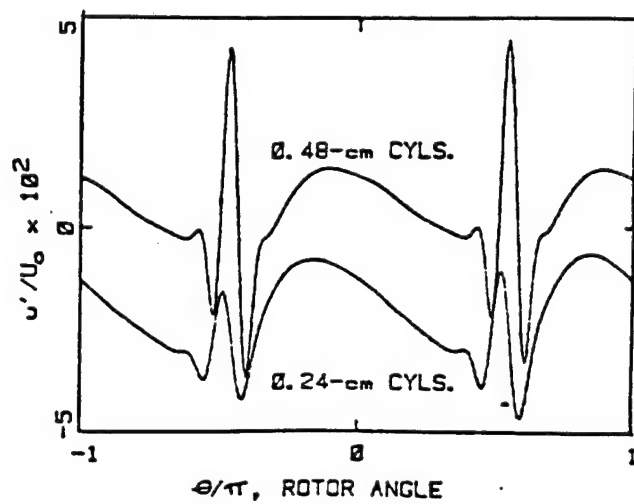
Fig.13 Experiment: Time signal $u'(t)/U_\infty$ observed at x=0.91 m near vertical location of maximum fluctuation. Upper curve for 0.48 cm rods, lower curve for 0.24 cm rods (5 × magnified).
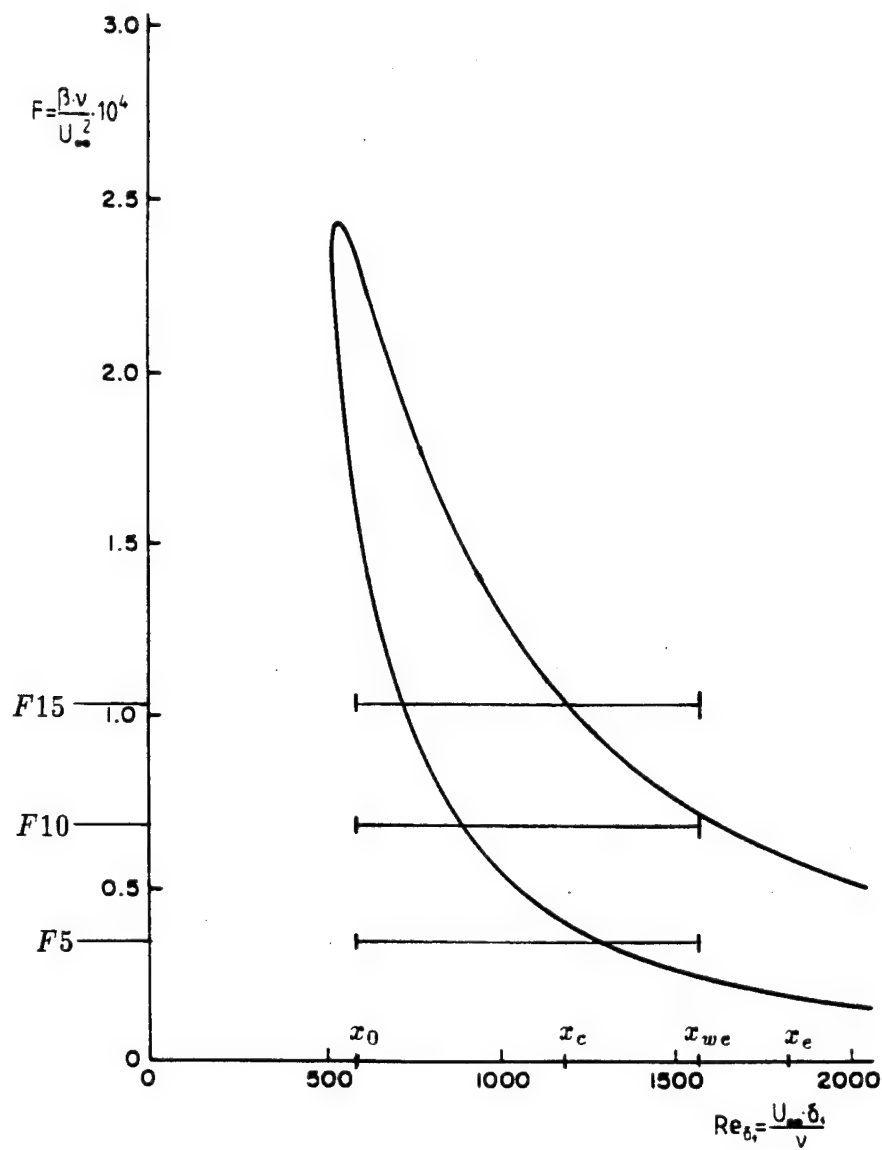
Fig.14. Neutral stability curve. Solution $\alpha_i = 0$ of the Orr-Sommerfeld equation for a zero pressure gradient, flat plate baseflow. Disturbances are amplified between the upper and lower branches of the neutral stability curve.

0.177E-02

X ←

-0.659E-03

U-AMPLITUDE, LAUF 1
MODE =   0

0.173E-01

0.000E+00

U-AMPLITUDE, LAUF 1
MODE =   1
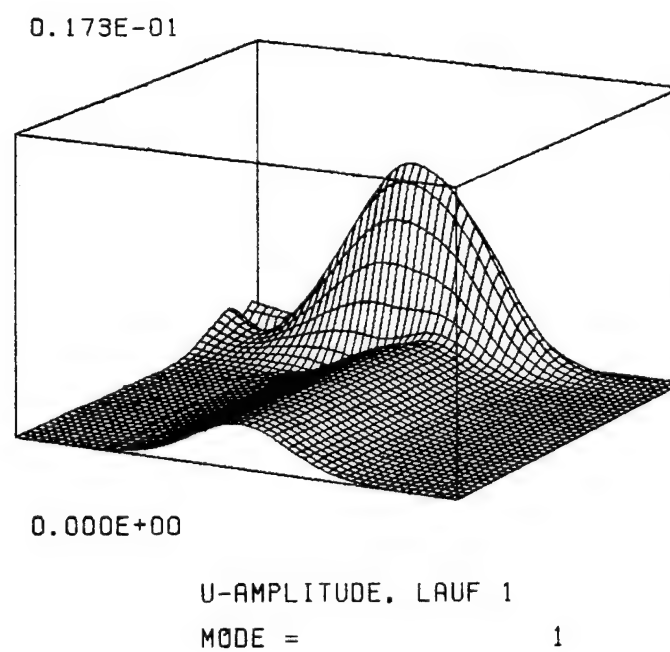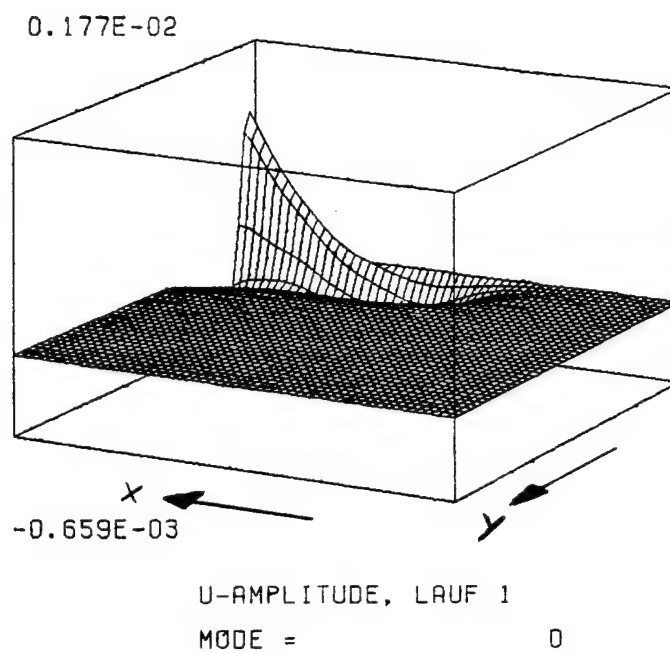
Fig.15. Fourier amplitudes of $u'(x,y)$ disturbances. Mean flow direction right to left, streamwise coordinate x.

0.108E-01
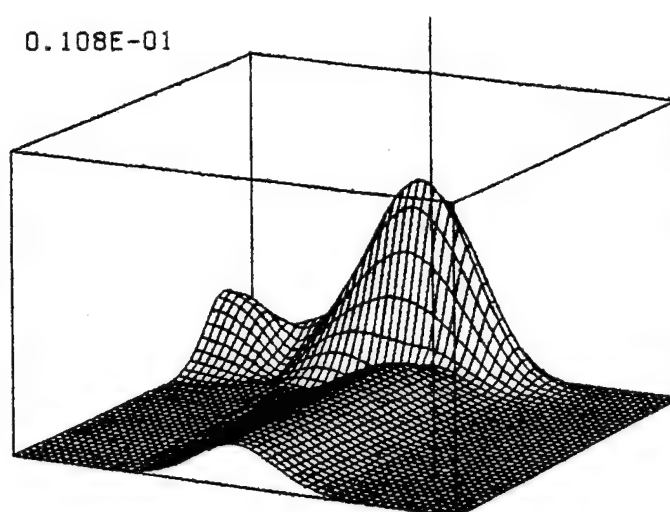
0.000E+00

U-AMPLITUDE, LAUF 1

MODE =   2

0.760E-02
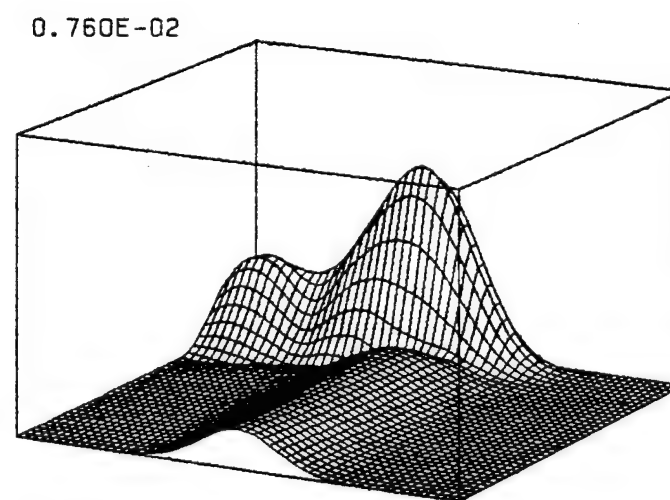
0.000E+00

U-AMPLITUDE, LAUF 1

MODE =   3

Fig.15. continued

0.611E-02
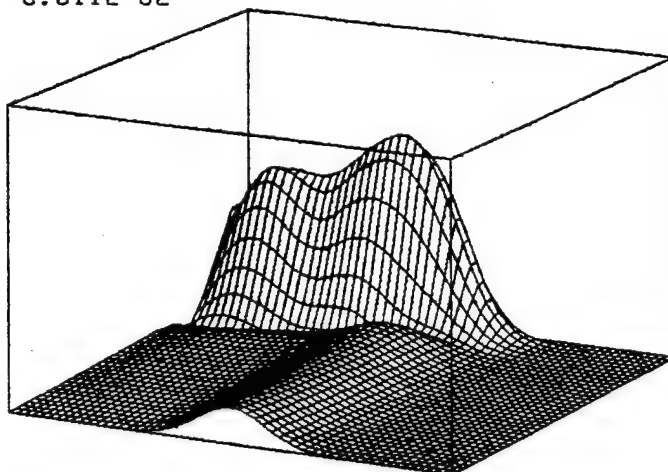
0.000E+00

U-AMPLITUDE, LAUF 1
MODE =   4

0.722E-02
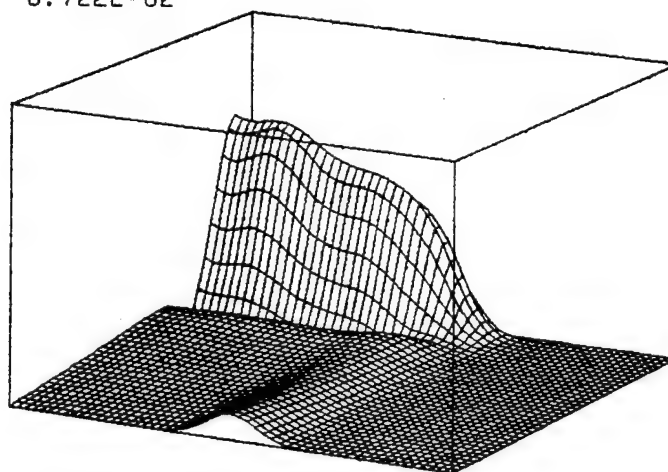
0.000E+00

U-AMPLITUDE, LAUF 1
MODE =   5

Fig.15. continued

0.143E-01
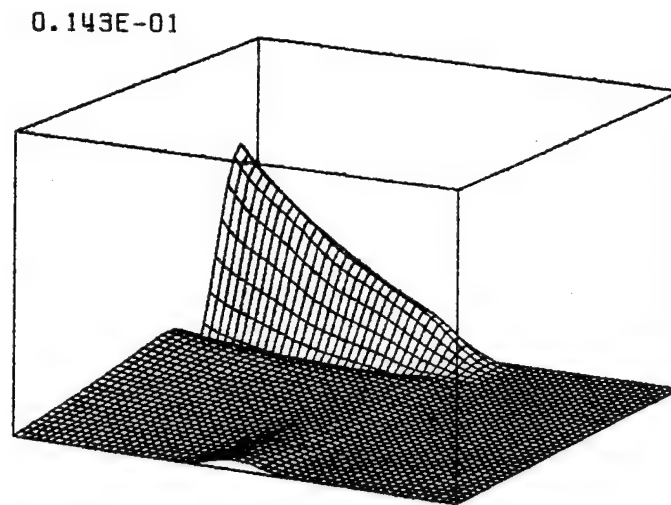
0.000E+00

U-AMPLITUDE, LAUF 1
MODE =   6

0.197E-01
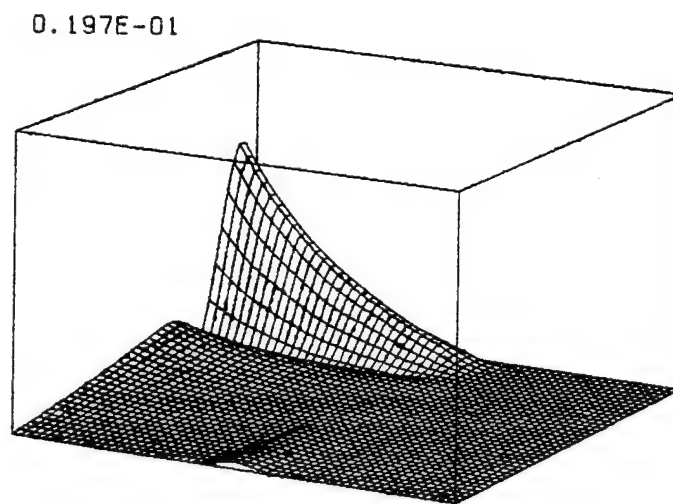
0.000E+00

U-AMPLITUDE, LAUF 1
MODE =   7

Fig.15. continued

0.223E-01

0.000E+00

U-AMPLITUDE, LAUF 1
MODE =   8

0.190E-01

0.000E+00

U-AMPLITUDE, LAUF 1
MODE =   9

Fig.15. continued

0.125E-01

0.000E+00

U-AMPLITUDE, LAUF 1
MODE =   10

0.670E-02

0.000E+00

U-AMPLITUDE, LAUF 1
MODE =   11

Fig.15. continued

0.372E-02
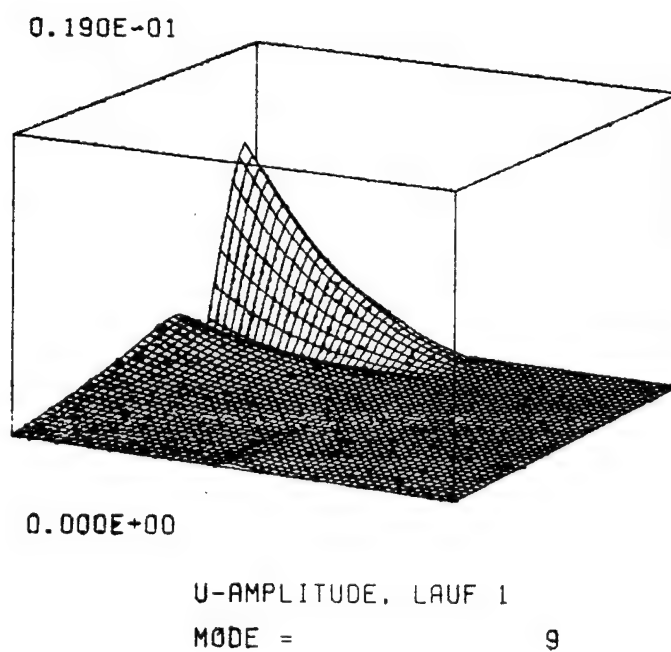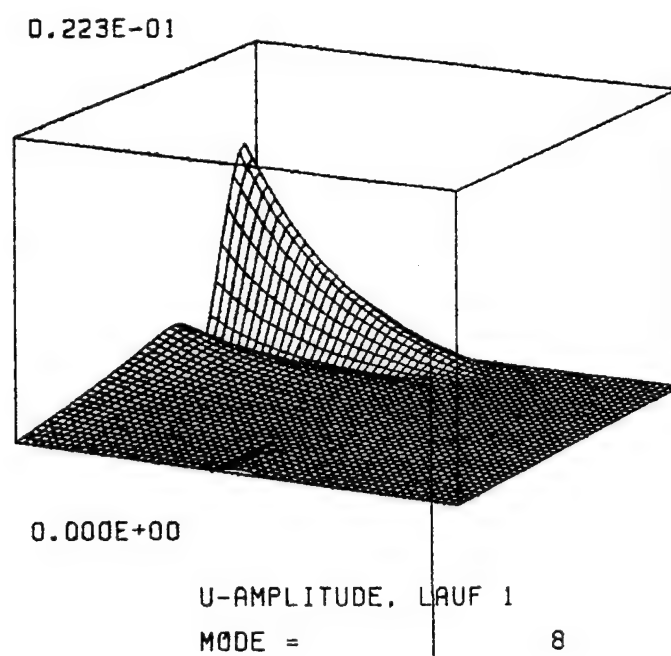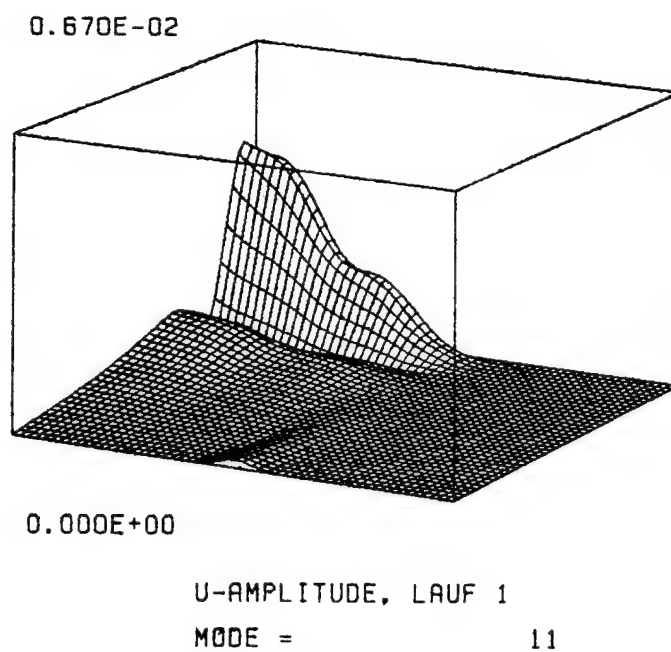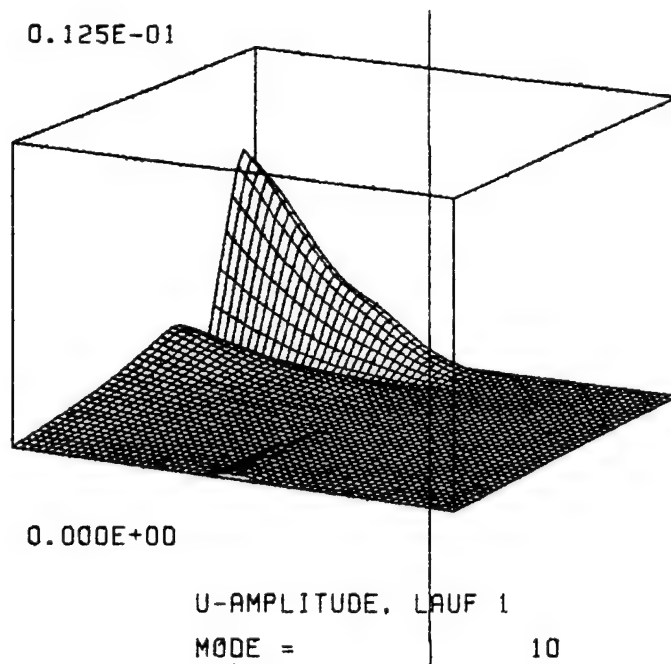
0.000E+00

U-AMPLITUDE, LAUF 1
MODE =   12

0.377E-02

0.000E+00

U-AMPLITUDE, LAUF 1
MODE =   13

Fig.15. continued

0.492E-02
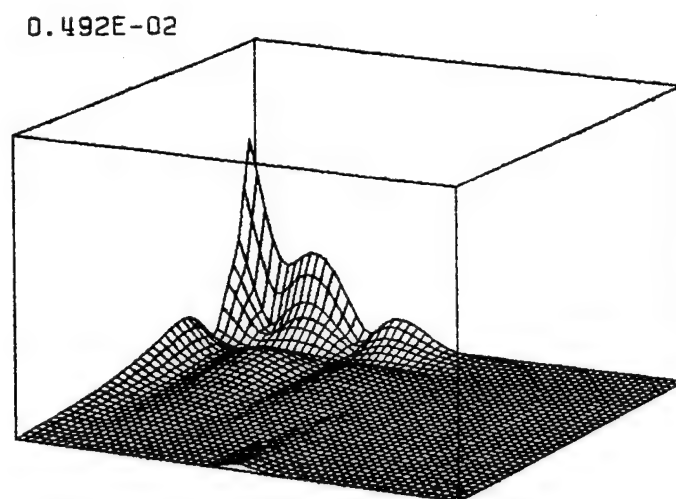
0.000E+00

U-AMPLITUDE. LAUF 1

MODE =   14

0.512E-02
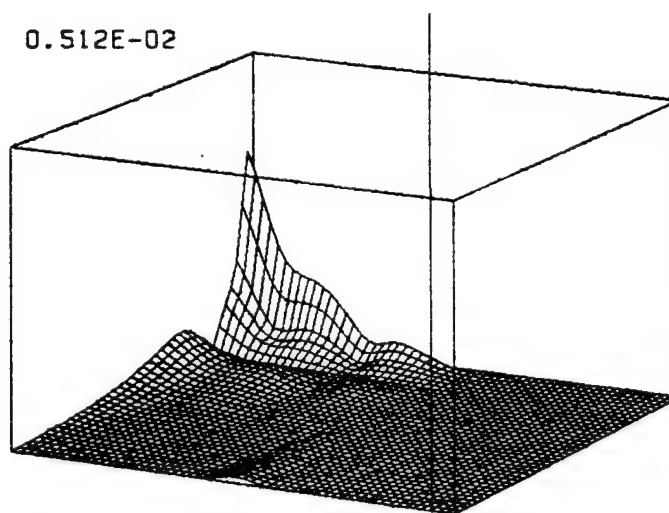
0.000E+00

U-AMPLITUDE. LAUF 1

MODE =   15

Fig.15. continued
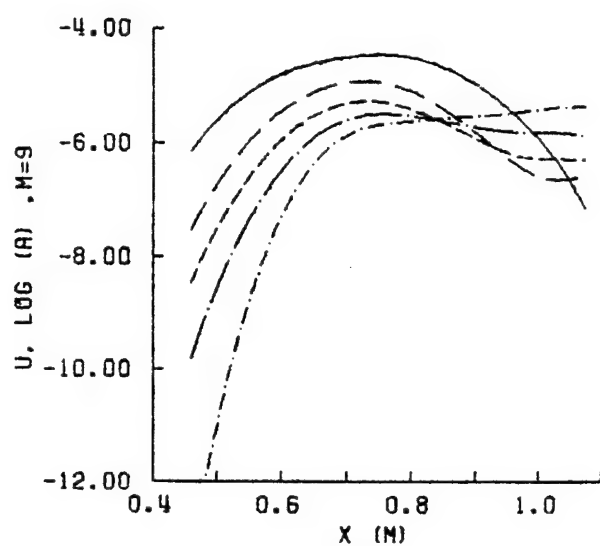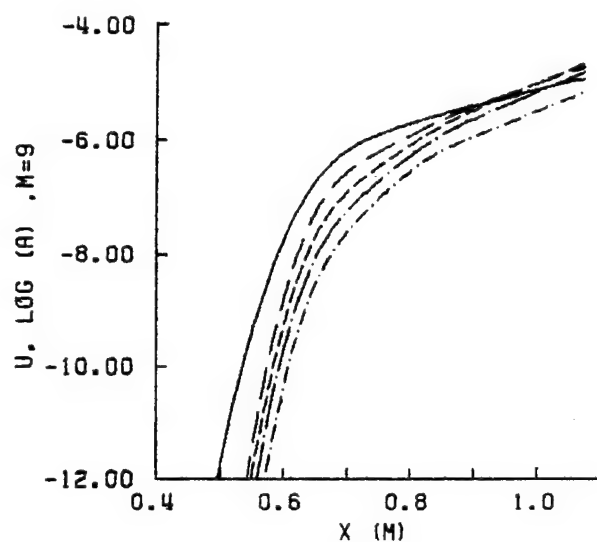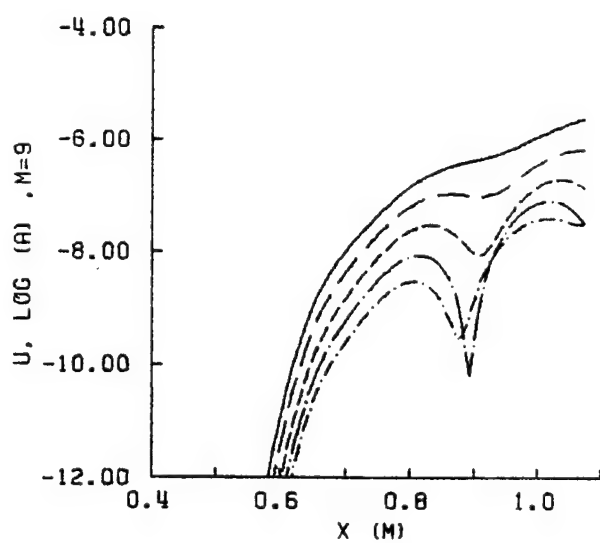
Fig.16. Numerical Simulation: Fourier amplitudes of u' disturbances inside boundary layer, observed at $m = 9$.
upper left: mode 1 - 5
upper right: mode 6 - 10
lower left: mode 11 - 15
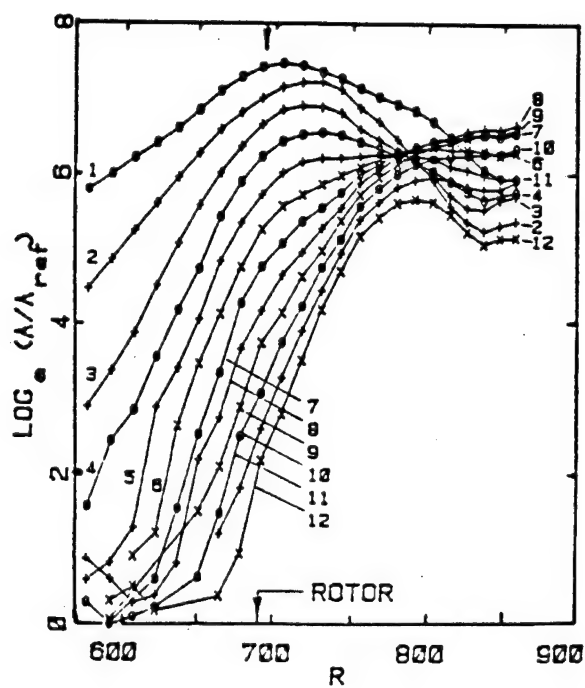
Fig.17. Experiment: Fourier amplitudes of induced disturbances.
Reference amplitude is arbitrary. R=550 corresponds to x=0.46 m
and R=850 to x=1.0 m $(R = \sqrt{Re_x})$.
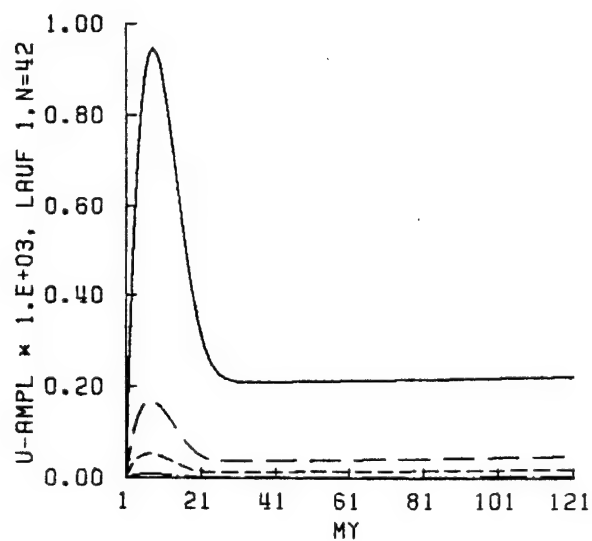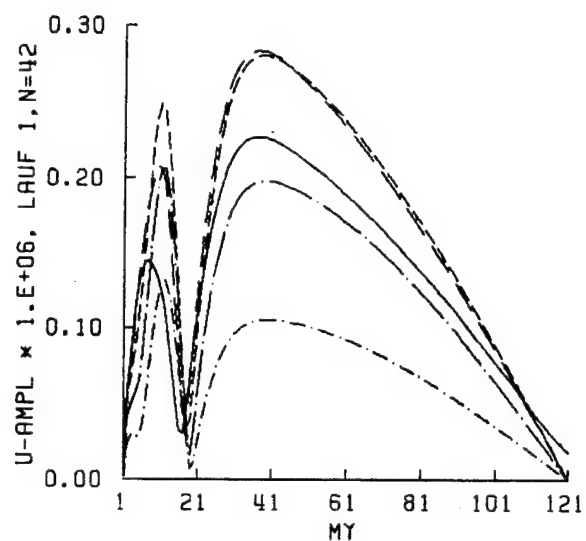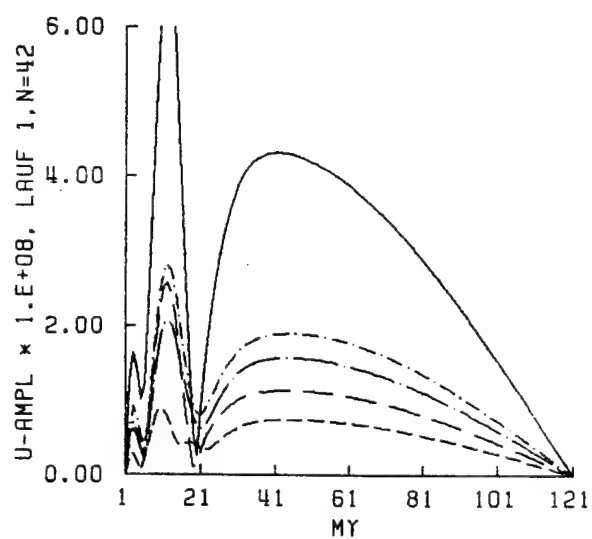
Fig.18a. Fourier amplitudes of $u'(y)$ at $n = 42$ (x=0.41 m).
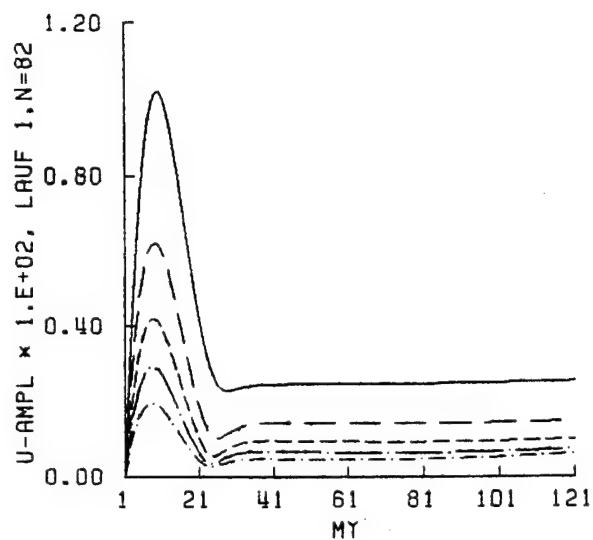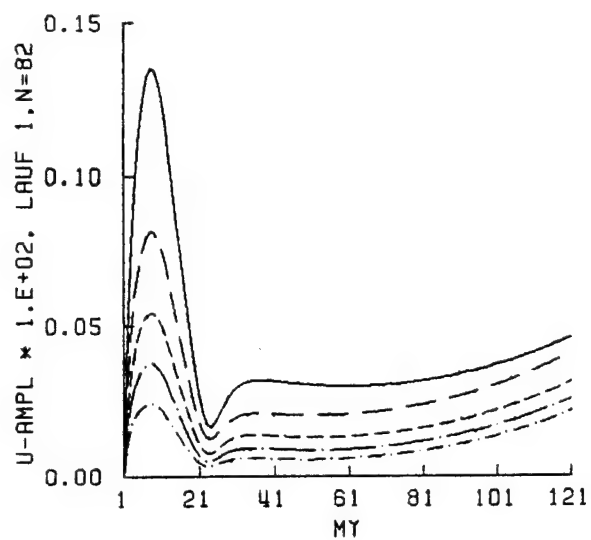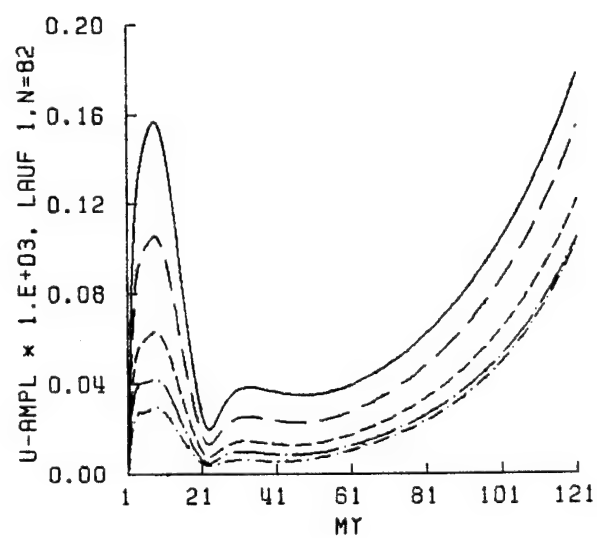
Fig.18b. Fourier amplitudes of $u'(y)$ at $n=82$ (x=0.66 m).
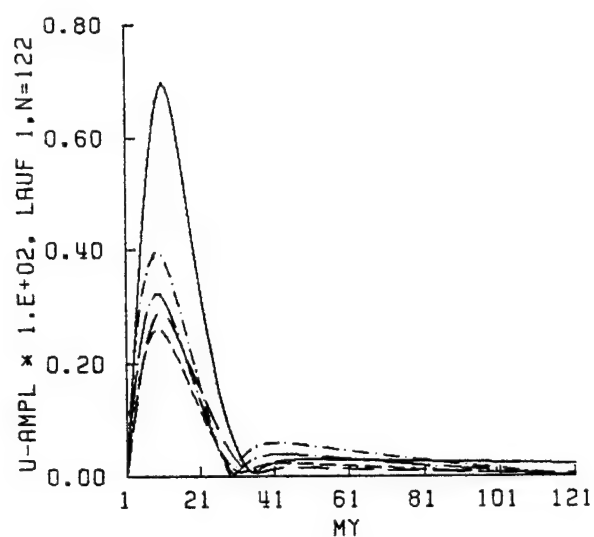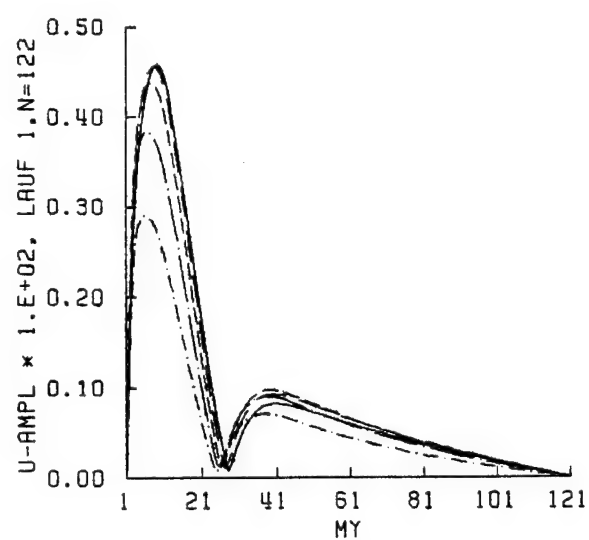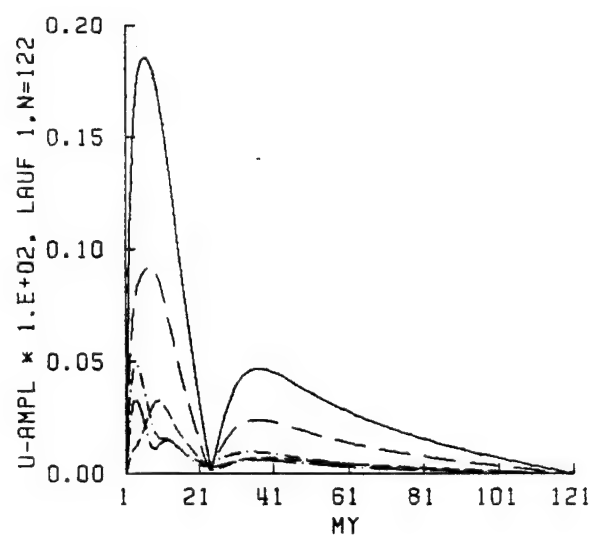
Fig.18c. Fourier amplitudes of $u'(y)$ at $n = 122$ (x=0.91 m).
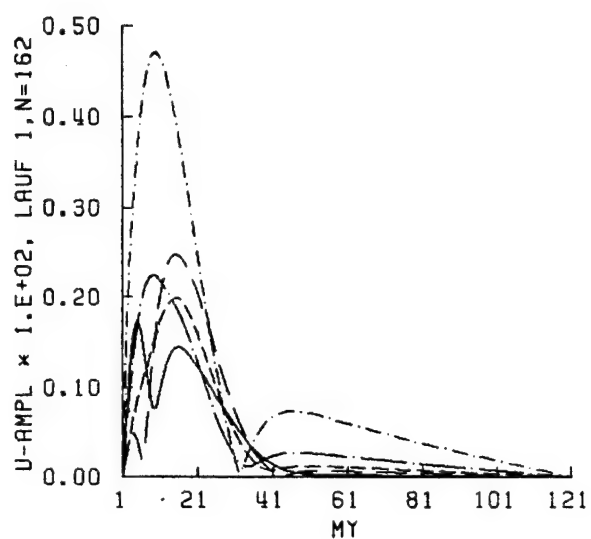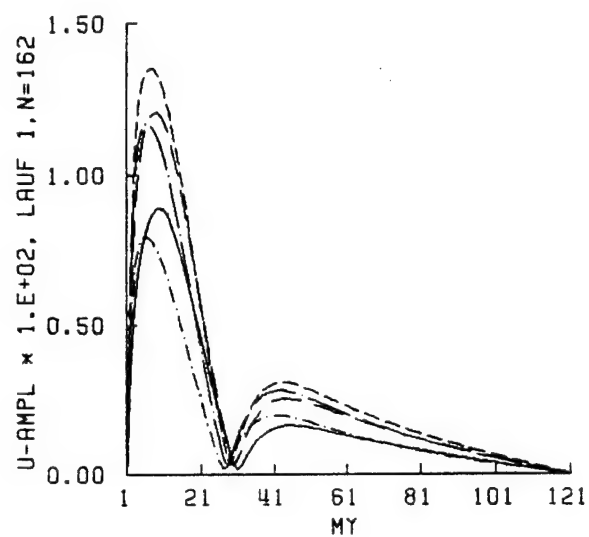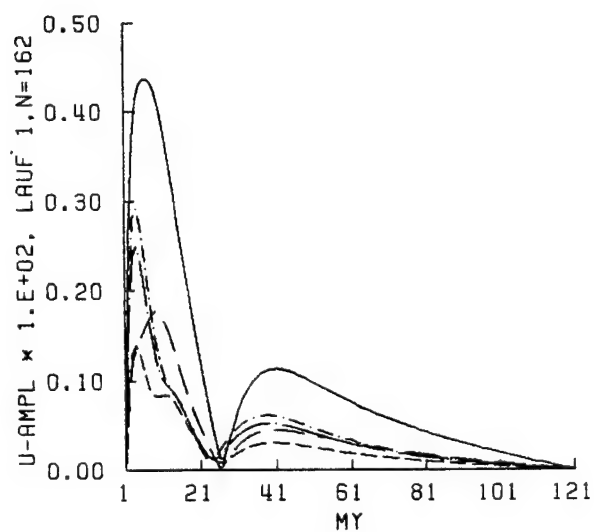
Fig.18d. Fourier amplitudes of $u'(y)$ at $n = 162$ (x=1.15 m).
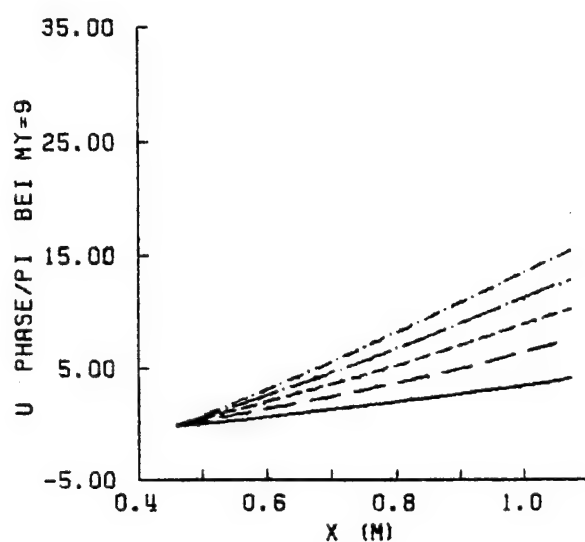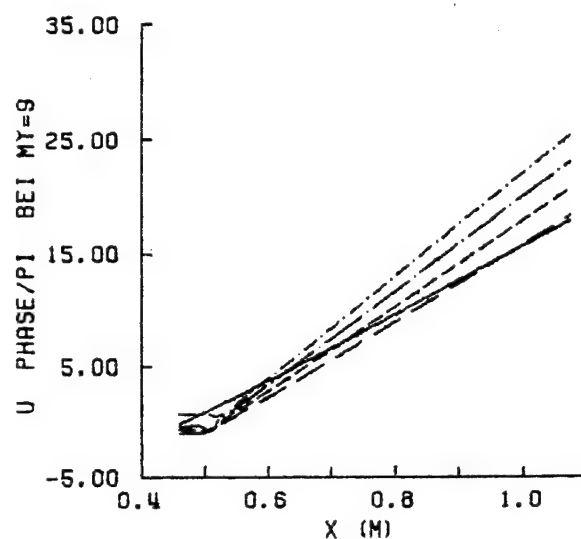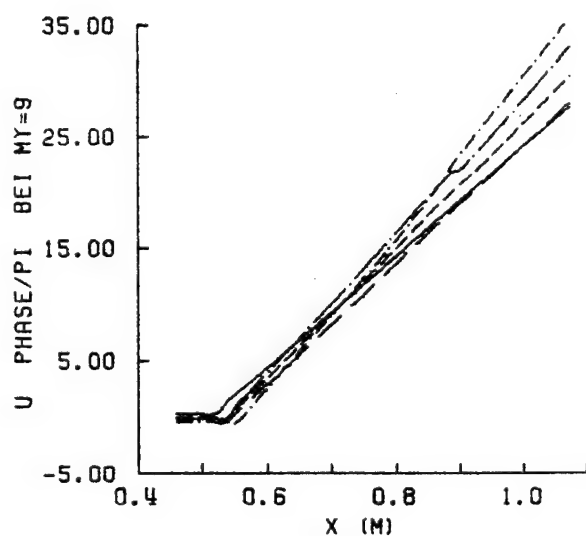
Fig.19. Phase development of $u'(x)$, corresponding to amplitudes of Fig.16. Phase data are divided by π. A steady phase growth in x indicates a finite phase speed of the disturbance wave.
upper left: mode 1 - 5
upper right: mode 6 - 10
lower left: mode 11 - 15
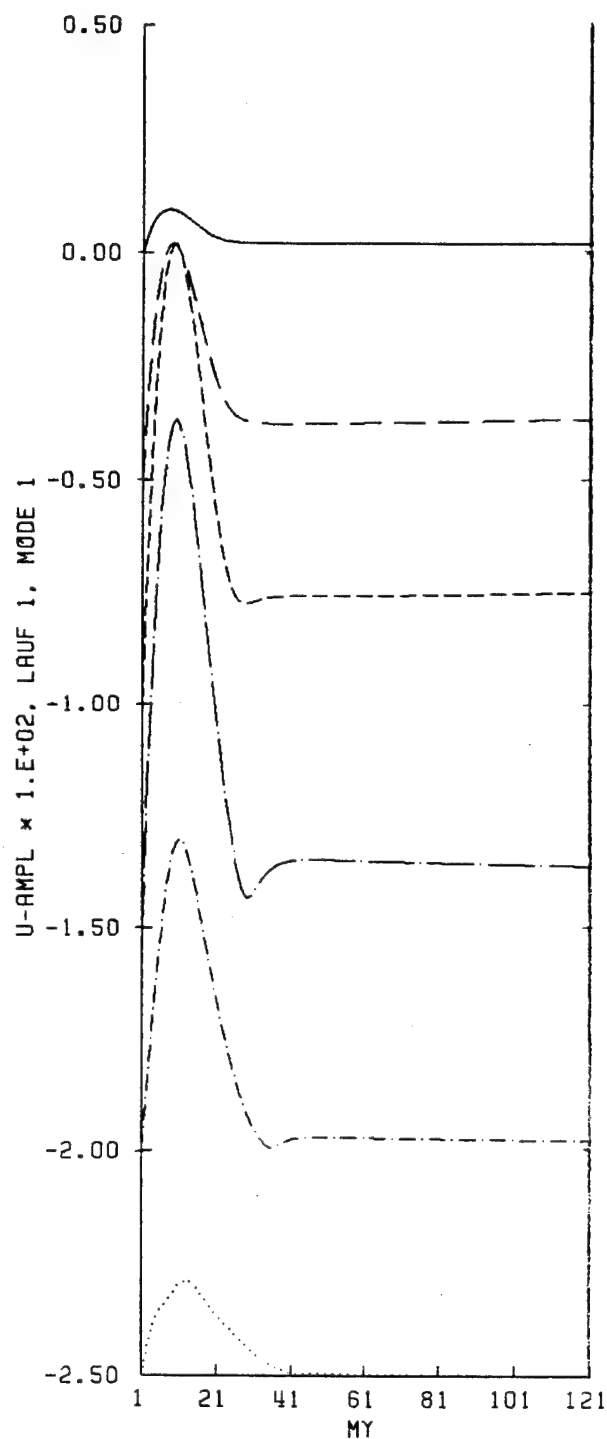
Fig.20. Fourier amplitudes of $u'(y)$ disturbance, mode 1. First station (top) at $n = 42$ (x=0.41 m). x-increments are 20 gridlines (12.3 cm). Vertical offset between successive baselines corresponds to u'$/U_\infty$ =0.5%.
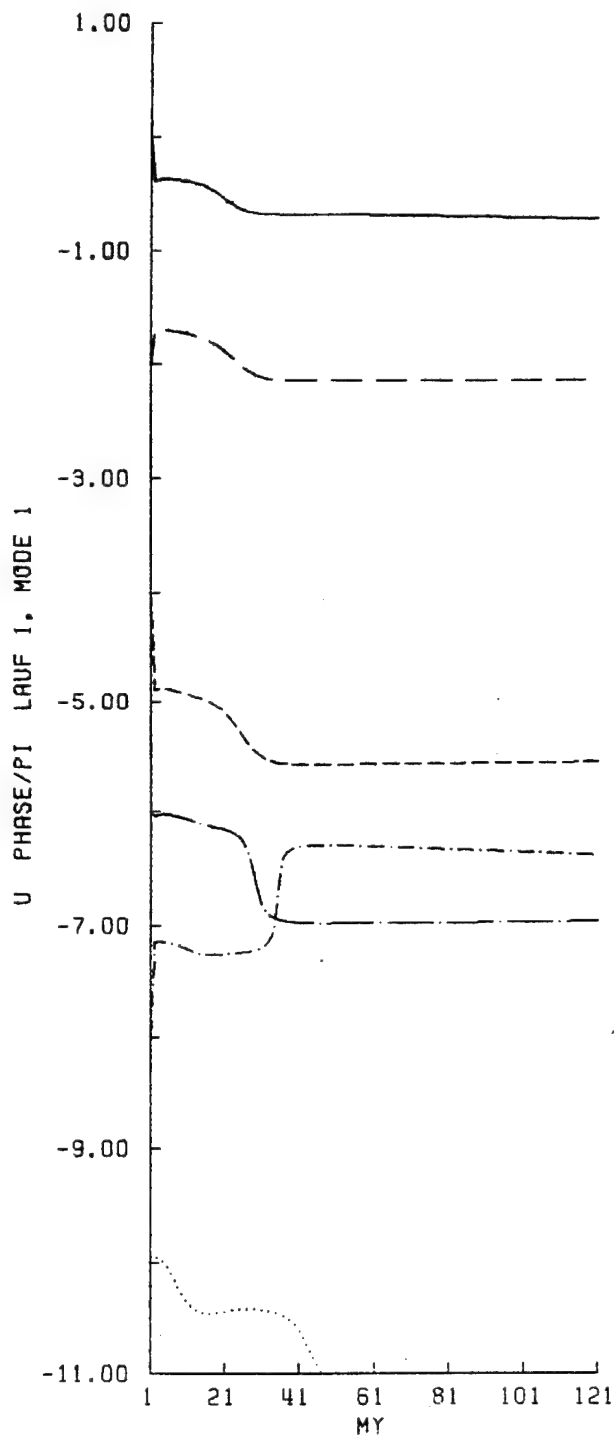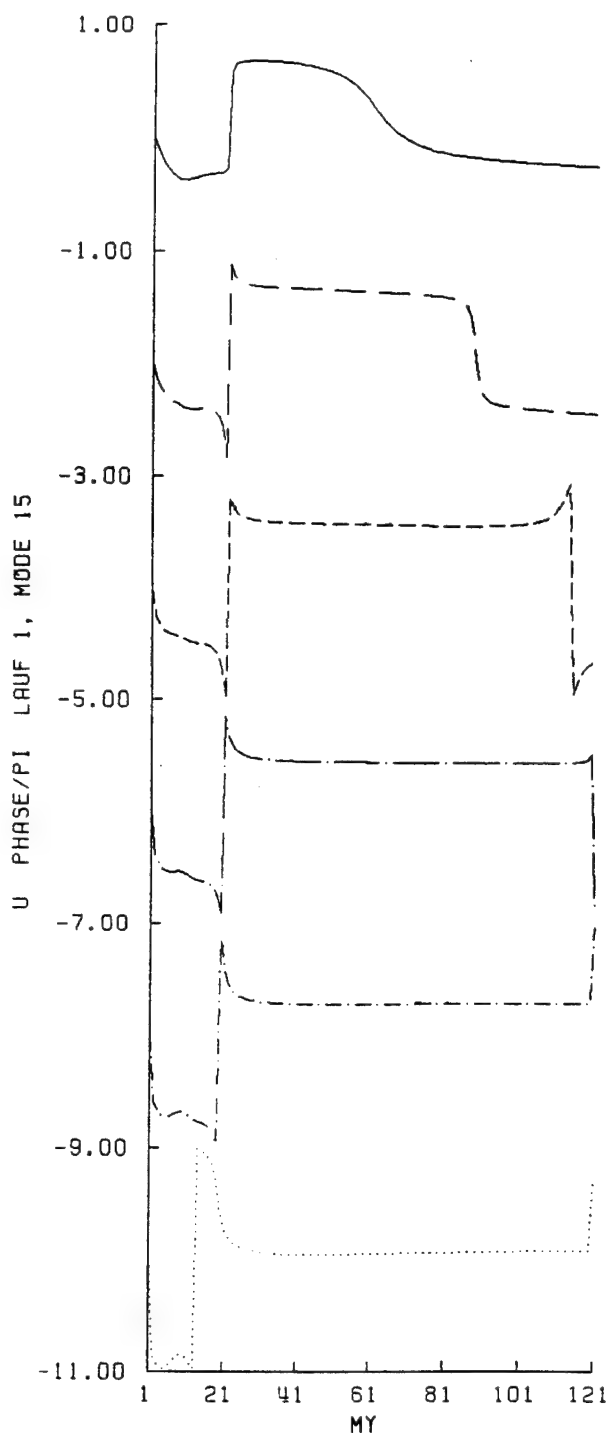
Fig.21. Phases of $u'(y)$, mode 1, evaluated together with amplitudes of Fig.20. Phase data are divided by π. Vertical offset between successive baselines corresponds to phase/π = 2.
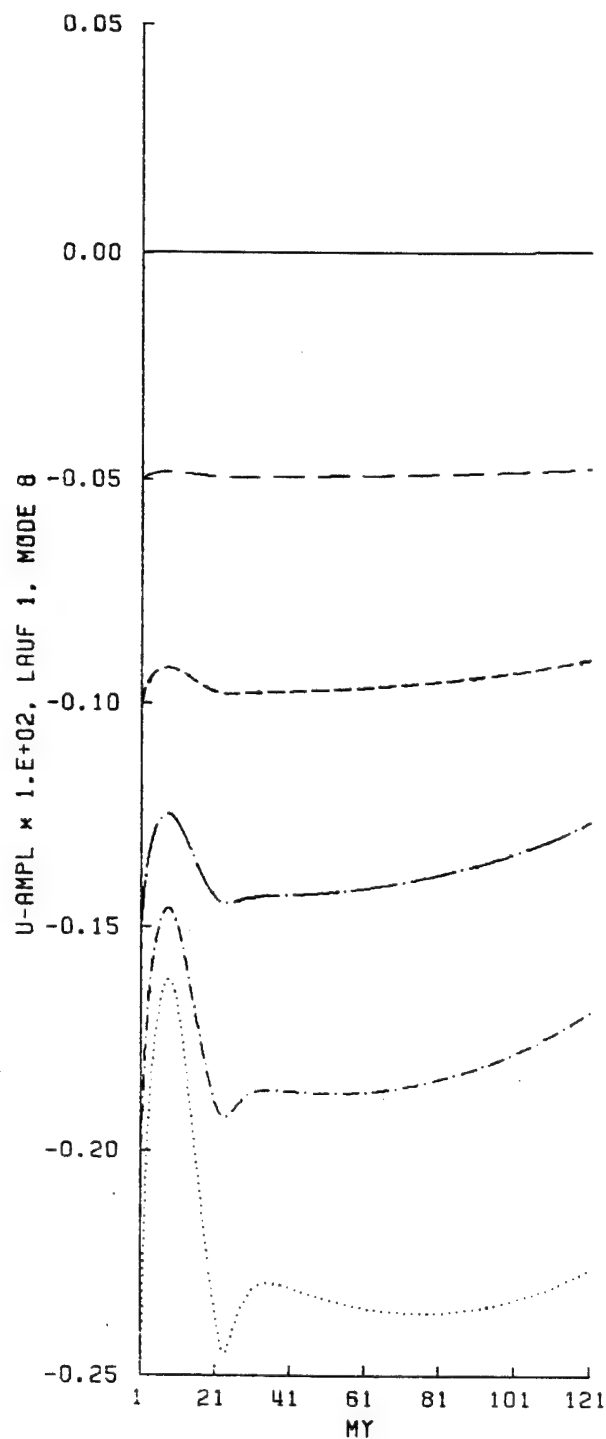
Fig.22a. Fourier amplitudes of $u'(y)$
disturbance, mode 8. First station
(top) at $n = 62$ (x=0.54 m). x-increments
are 5 gridlines (3 cm). Vertical off-
set between successive baselines corre-
sponds to u'/U_∞ = 0.05%.
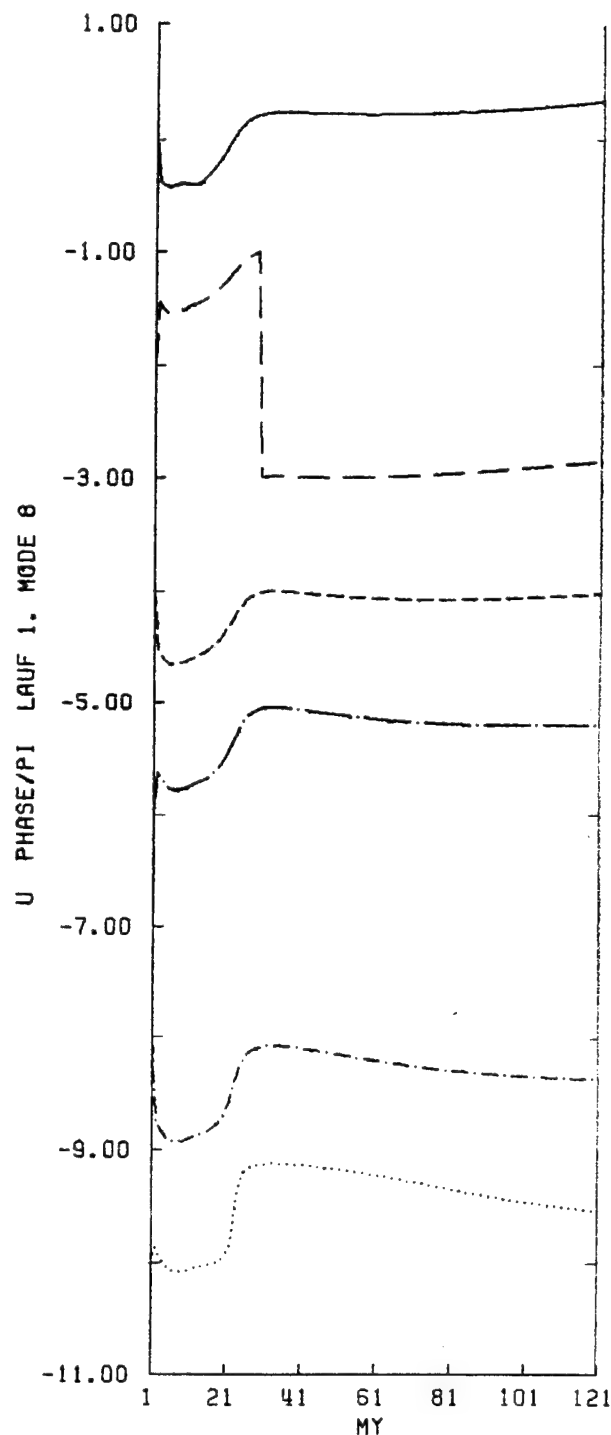
Fig.23a. Phases of $u'(y)$, mode 8,
evaluated together with amplitudes of
Fig.22a. First station (top) at $n = 62$
(x=0.54 m). x-increments are 5 grid-
lines (3 cm). Phase data are divided by
π. Vertical offset between successive
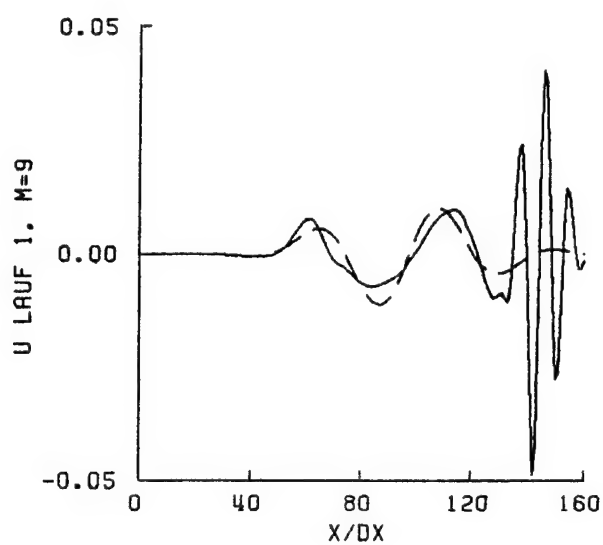baselines corresponds to phase/$\pi = 2$.
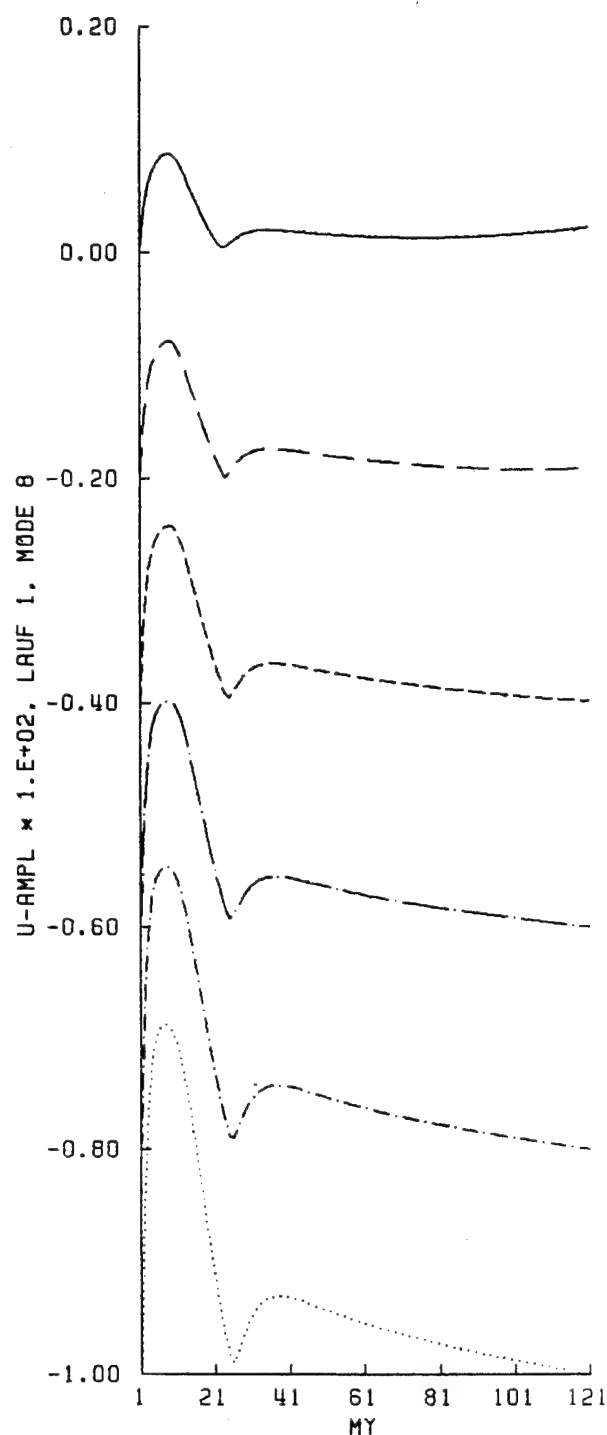
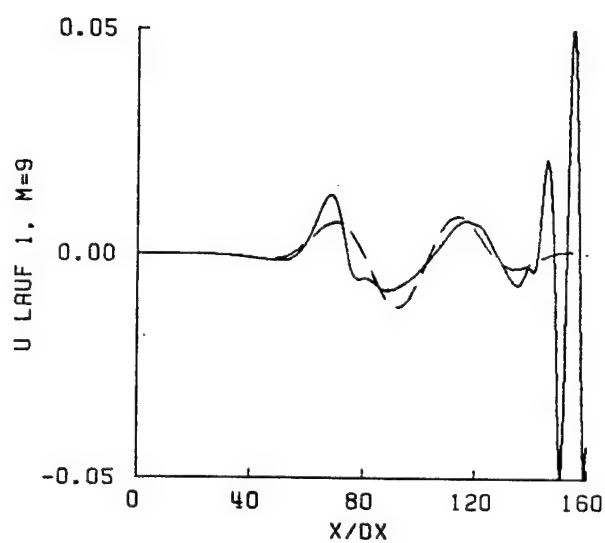Fig.22b. Fourier amplitudes of $u'(y)$ disturbance, mode 8. First station (top) at $n=87$ (x=0.69 m). x-increments are 5 gridlines (3 cm). Vertical offset between successive baselines corresponds to u'/U_∞ = 0.2%.
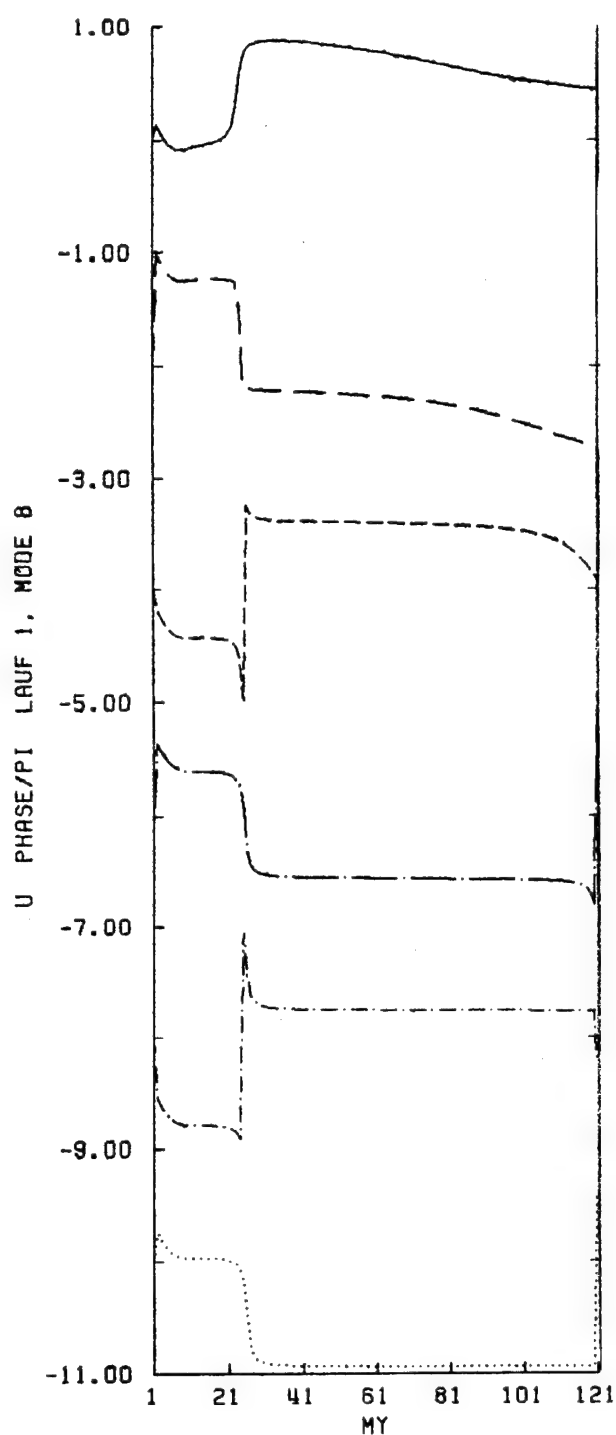
Fig.23b. Phases of $u'(y)$, mode 8, evaluated together with amplitudes of Fig.22b. First station (top) at $n=87$ (x=0.69 m). x-increments are 5 gridlines (3 cm). Phase data are divided by π. Vertical offset between successive baselines corresponds to phase/π=2.
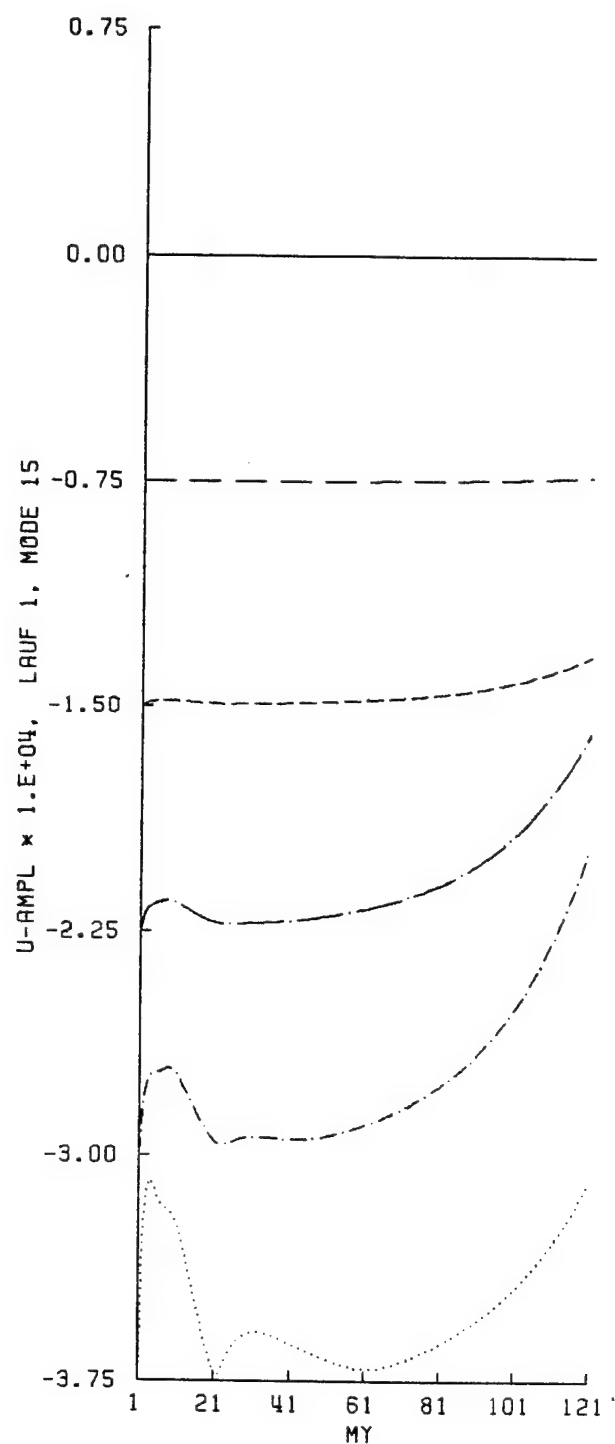
Fig.24a. Fourier amplitudes of $u'(y)$ disturbance, mode 15. First station (top) at $n=62$ (x=0.54 m). x-increments are 5 gridlines (3 cm). Vertical offset between successive baselines corresponds to u'/U_∞ = 0.75 × 10^{-4}.
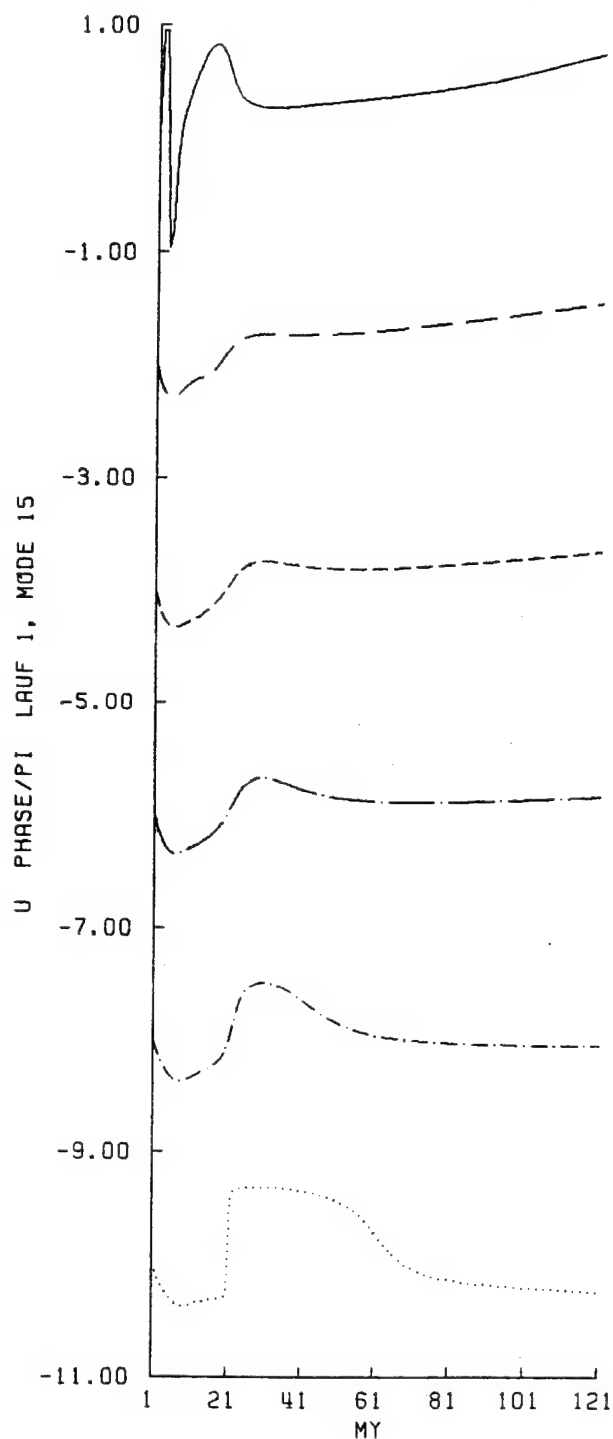
Fig.25a. Phases of $u'(y)$, mode 15, evaluated together with amplitudes of Fig.24a. First station (top) at $n=62$ (x=0.54 m). x-increments are 5 gridlines (3 cm). Phase data are divided by π. Vertical offset between successive baselines corresponds to phase/$\pi=2$.
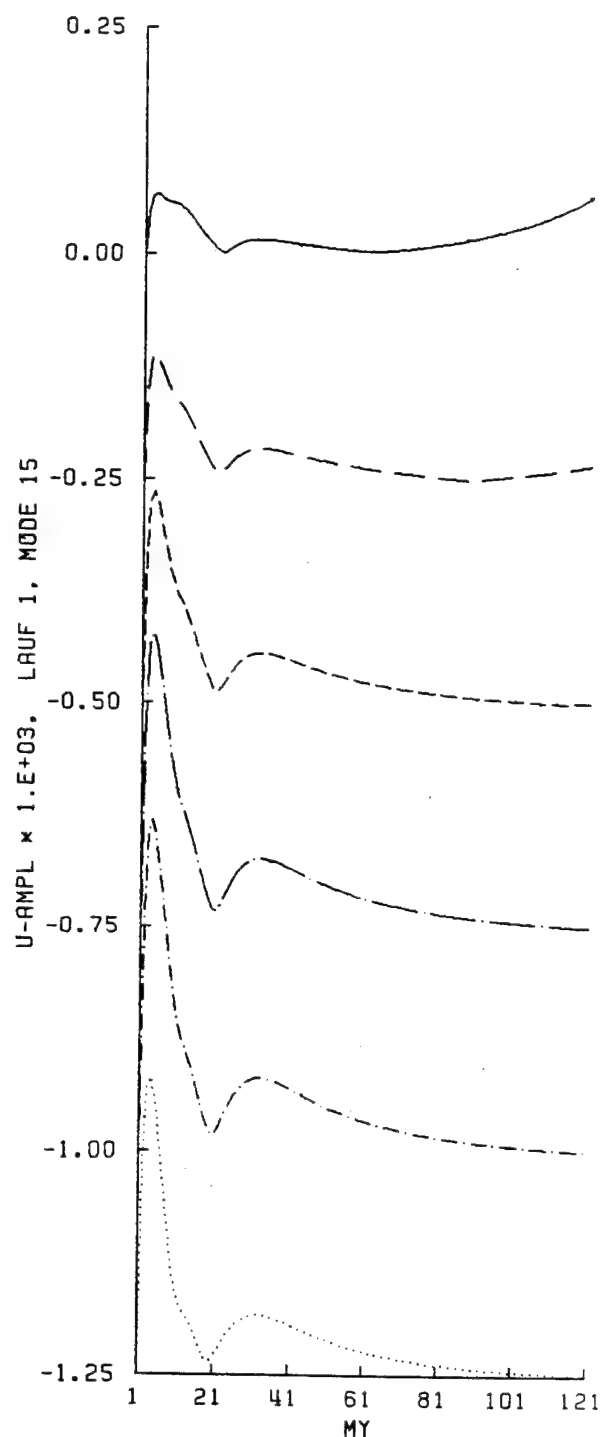
Fig.24b. Fourier amplitudes of $u'(y)$ disturbance, mode 15. First station (top) at $n=87$ (x=0.69 m). x-increments are 5 gridlines (3 cm). Vertical offset between successive baselines corresponds to u'/U_∞ = 0.25 × 10^{-3}.

Fig.25b. Phases of $u'(y)$, mode 15, evaluated together with amplitudes of Fig.24b. First station (top) at $n=87$ (x=0.69 m). x-increments are 5 gridlines (3 cm). Phase data are divided by π. Vertical offset between successive baselines corresponds to phase/$\pi=2$.
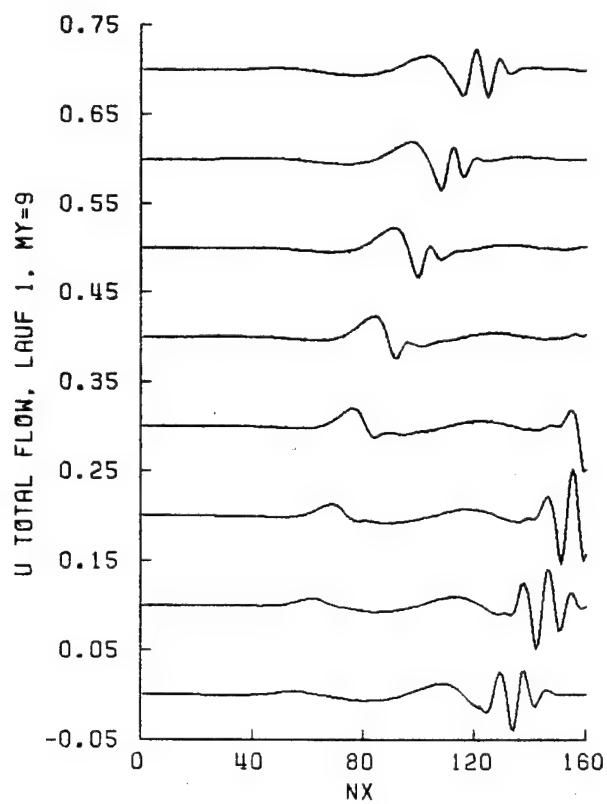
Fig.26. Disturbance velocity $u'(x)$, total fluctuation. $NX = 1$ corresponds to x=0.16 m, $NX = 160$ corresponds to x=1.14 m. First station (bottom) recorded at $t = 1$, increments are 32 timesteps. 1 period = 256 timesteps. Vertical offset between successive baselines corresponds to $u'/U_\infty = 0.1$
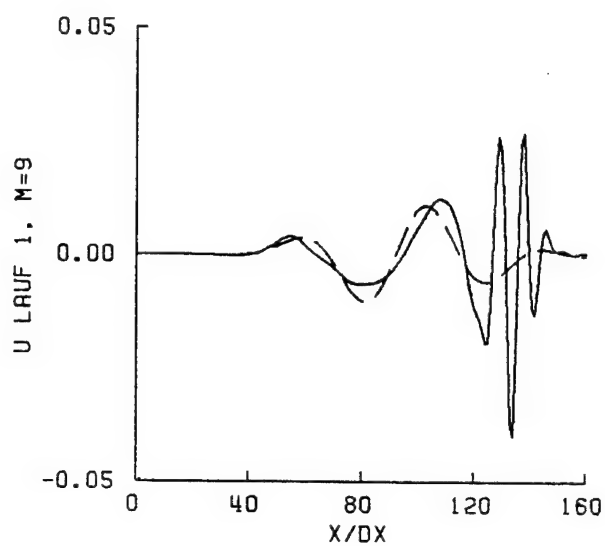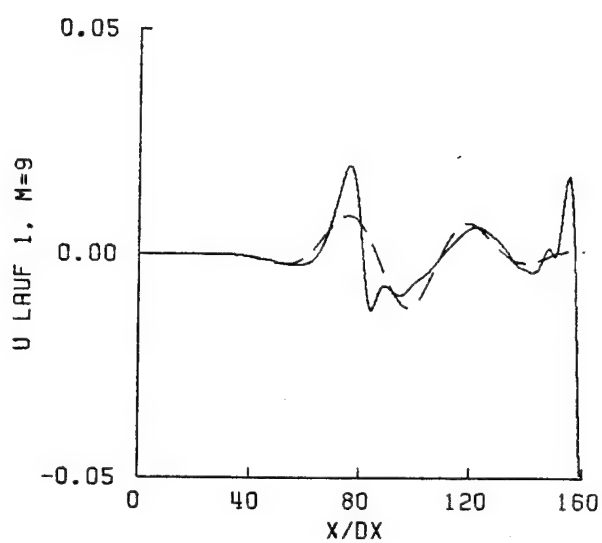
Fig.27. Disturbance velocity $u'(x)$, total fluctuation vs. mode 1 fluctuation.
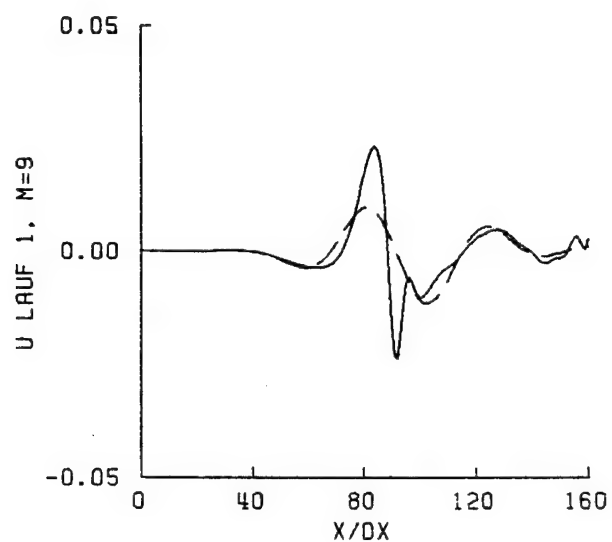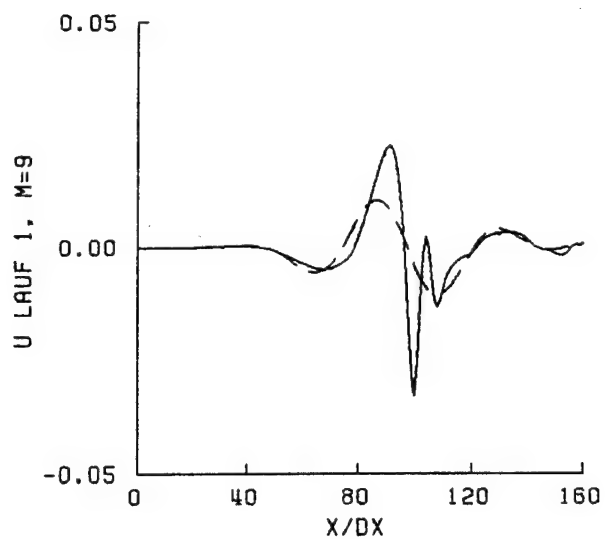
Fig.27. continued

baseflow + wave trough = unstable profile
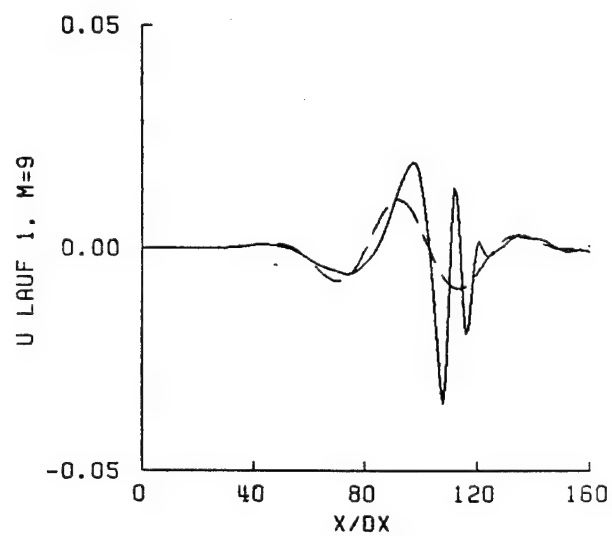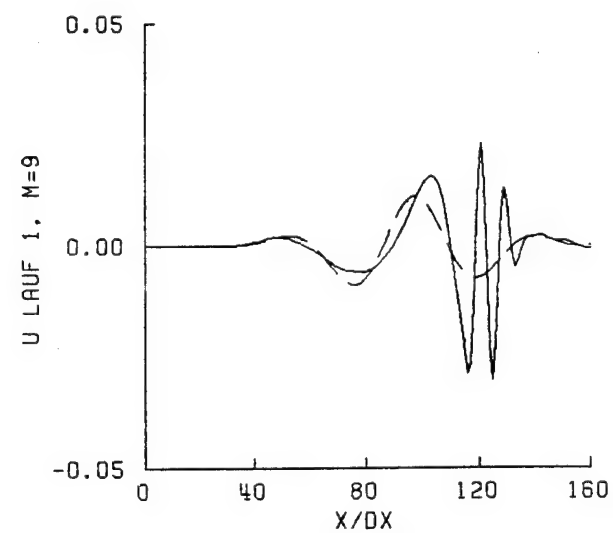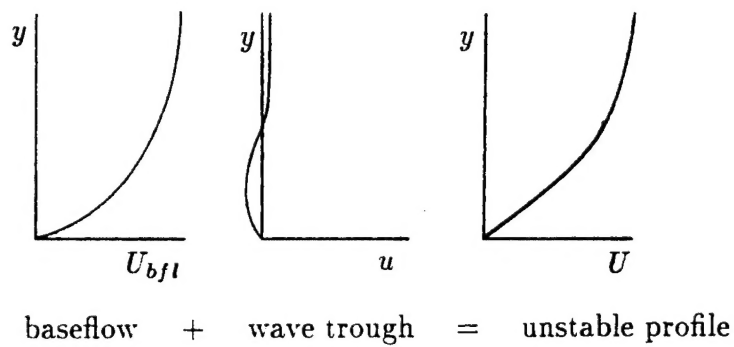
Fig.28a. Superposition of steady baseflow and low mode wave trough to form a destabilizing velocity profile.

baseflow + wave crest = stable profile
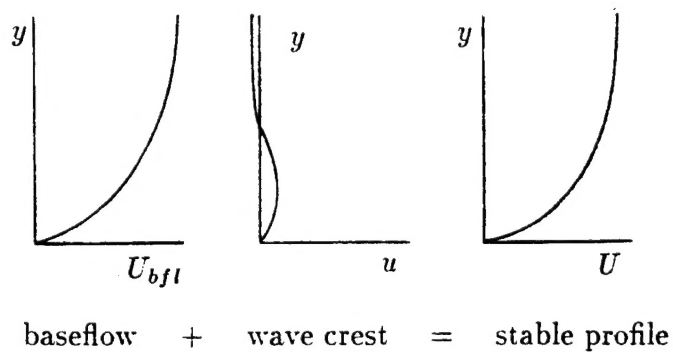
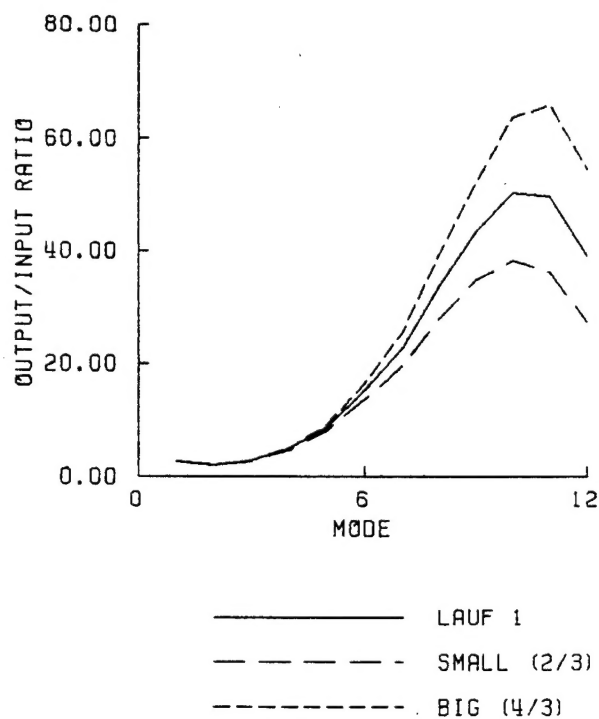Fig.28b. Superposition of steady baseflow and low mode wave crest to form a stabilizing velocity profile.

Fig.29. Numerical simulation: Output/input ratio for three cases: Reference case (=Lauf 1), smaller amplitudes (=Small 2/3), higher amplitudes (=Big 4/3). Input amplitudes: u' at $(m=51, n=82)$ underneath rotor. Output amplitudes: u' at $(m=9, n=122)$.
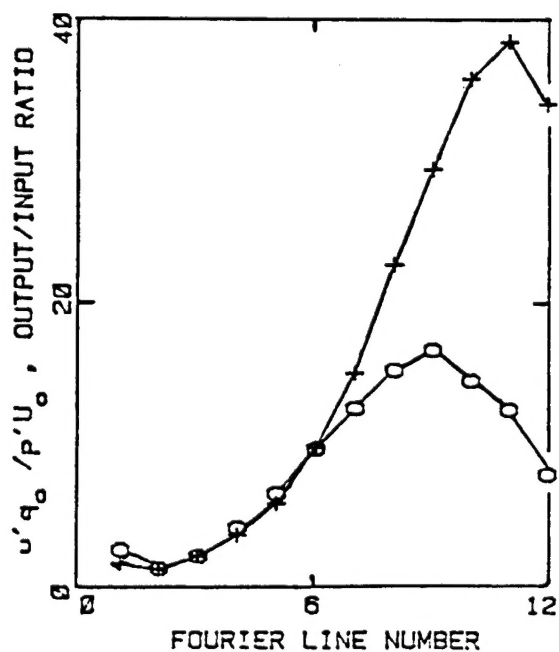
Fig.30. Experiment: Output/input ratio for two rod diameters: 0.48 cm (+) and 0.32 cm (o). Input amplitudes: Normalized pressure p'/q_0 underneath rotor. Output amplitudes: u'/U_∞ at 0.91 m.
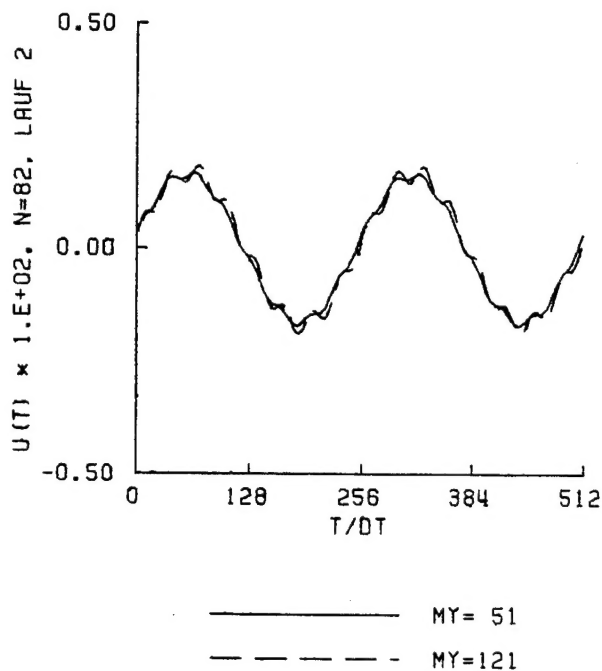

Fig.31. Time signal of forcing with modes $1 + 8$ only, at $n = 82$ (x=0.66 m). Disturbance velocity u' plotted over two periods. $m = 121$ is at the freestream boundary, $m = 51$ is at about two boundary layer thicknesses.
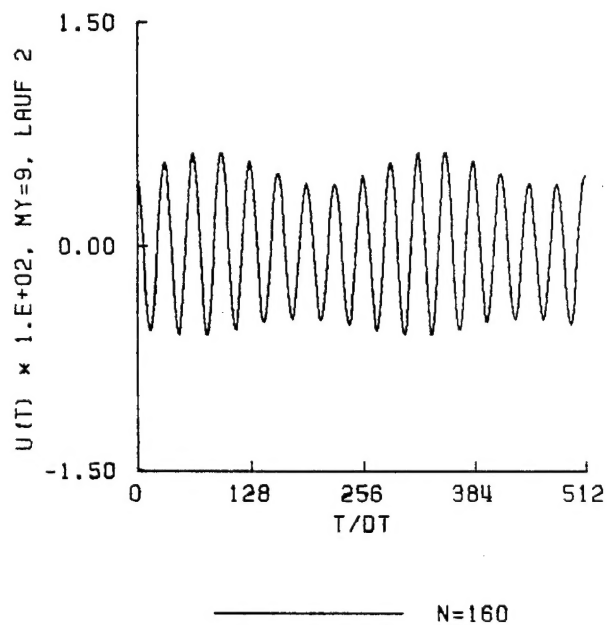
Fig.32. Time signal $u'(t)$ observed at $n = 160$ (x=1.14 m) near vertical location of maximum fluctuation.
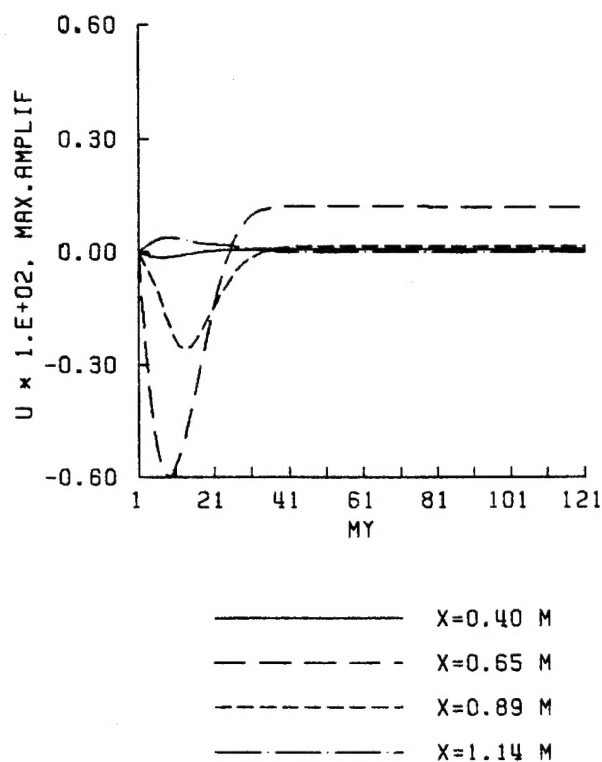
Fig.33a. Mode 1 profiles, superimposed on steady baseflow to form destabilizing transient baseflow profiles.
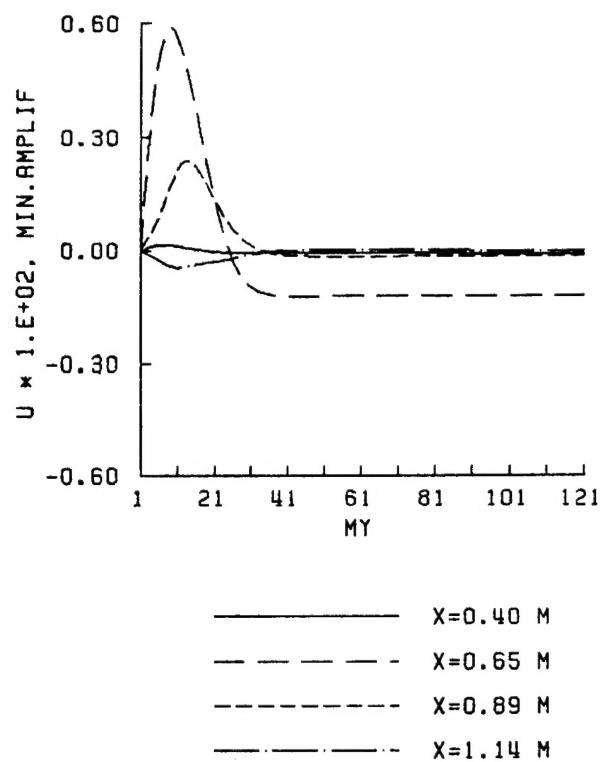

Fig.33b. Mode 1 profiles, superimposed on steady baseflow to form stabilizing transient baseflow profiles.
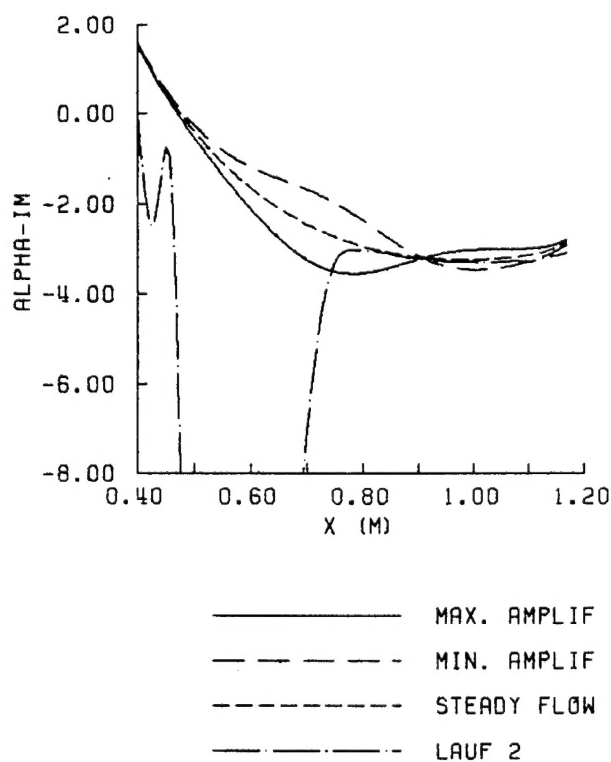

Fig.34. $\alpha_i(x)$ for four cases, forcing with reference amplitudes:

(1.) Maximum amplification of a TS wave traveling in a wave trough, according to linear stability theory.

(2.) Minimum amplification of a TS wave traveling in a wave crest, according to linear stability theory.

(3.) Amplification of a TS wave in steady baseflow, according to linear stability theory.

(4.) $\alpha_i(x)$ computed from the Fourier amplitudes of Navier-Stokes simulation.